



# A locally adaptive $L_1 - L_2$ norm for multi-frame super-resolution of images with mixed noise and outliers

Linwei Yue<sup>a</sup>, Huanfeng Shen<sup>b</sup>, Qiangqiang Yuan<sup>c</sup>, Liangpei Zhang<sup>a,\*</sup>

<sup>a</sup> The State Key Laboratory of Information Engineering in Surveying, Mapping and Remote Sensing, Wuhan University, Wuhan, PR China

<sup>b</sup> School of Resource and Environmental Science, Wuhan University, Wuhan, PR China

<sup>c</sup> School of Geodesy and Geomatics, Wuhan University, Wuhan, PR China

## ARTICLE INFO

### Article history:

Received 22 December 2013

Received in revised form

24 April 2014

Accepted 25 April 2014

Available online 6 May 2014

### Keywords:

Super-resolution

Adaptive norm

Mixed noise

Motion outliers

Adaptive weight estimation

## ABSTRACT

In this paper, we present a locally adaptive regularized super-resolution model for images with mixed noise and outliers. The proposed method adaptively assigns the local norms in the data fidelity term of the regularized model. Specifically, it determines different norm values for different pixel locations, according to the impulse noise and motion outlier detection results. The  $L_1$  norm is employed for pixels with impulse noise and motion outliers, and the  $L_2$  norm is used for the other pixels. In order to balance the difference in the constraint strength between the  $L_1$  norm and the  $L_2$  norm, a strategy to adaptively estimate a weighted parameter is put forward. The experimental results confirm the superiority of the proposed method for different images with mixed noise and outliers.

© 2014 Elsevier B.V. All rights reserved.

## 1. Introduction

Due to the limitation of solid-state sensors such as CCD or CMOS, the digital images acquired may have a limited spatial resolution, thus reduce their practical value. In addition, digital images may be degraded by blurring or noise because the information each pixel records is easily polluted during the acquisition and transmission procedure. Super-resolution is a technique which takes resolution limitation and regular image degradation into consideration at the same time. Using the redundant information between multi-frame images with a relative sub-pixel motion, the super-resolution technique can construct a higher-resolution image or sequence, and it has been widely applied with medical images [1], remote sensing images [2–4], and video surveillance [5,6].

The multi-frame super-resolution technique has been developed for almost three decades [7]. The frequency domain approaches were first addressed; however, these

methods [7–9] are extremely sensitive to model errors, and have difficulty in including prior knowledge to solve the model. Therefore, methods in the spatial domain have become more popular in recent years [3,10–13]. These methods include iterative back projection (IBP) [10], projection onto convex sets (POCS) [11], and a group of Bayesian-based probability and statistical methods [3,12,13]. Among the methods, the Bayesian-based methods have the advantages of adding a prior and simultaneously handling the high-resolution (HR) image estimation. Furthermore, the model parameters such as the motion vector and blur kernel are estimated iteratively [12]. As a result, the Bayesian-based methods have become the most widely used. These methods in the spatial domain regard super-resolution as an ill-posed inverse problem. Supposing the degradation procedure during image acquisition involves warping, blurring, downsampling, and noise (Fig. 1), then the universal observation model is usually described as follows [14,15]:

$$\mathbf{y}_k = \mathbf{D}_k \mathbf{B}_k \mathbf{M}_k \mathbf{z} + \mathbf{n}_k \quad (1)$$

where  $\mathbf{y}_k$  is the  $k$ th observed image of size  $n_1 \times n_2$ , and  $\mathbf{z}$  is the desired HR image of size  $N_1 \times N_2$ , which is determined

\* Corresponding author.

E-mail address: [zlp62@whu.edu.cn](mailto:zlp62@whu.edu.cn) (L. Zhang).

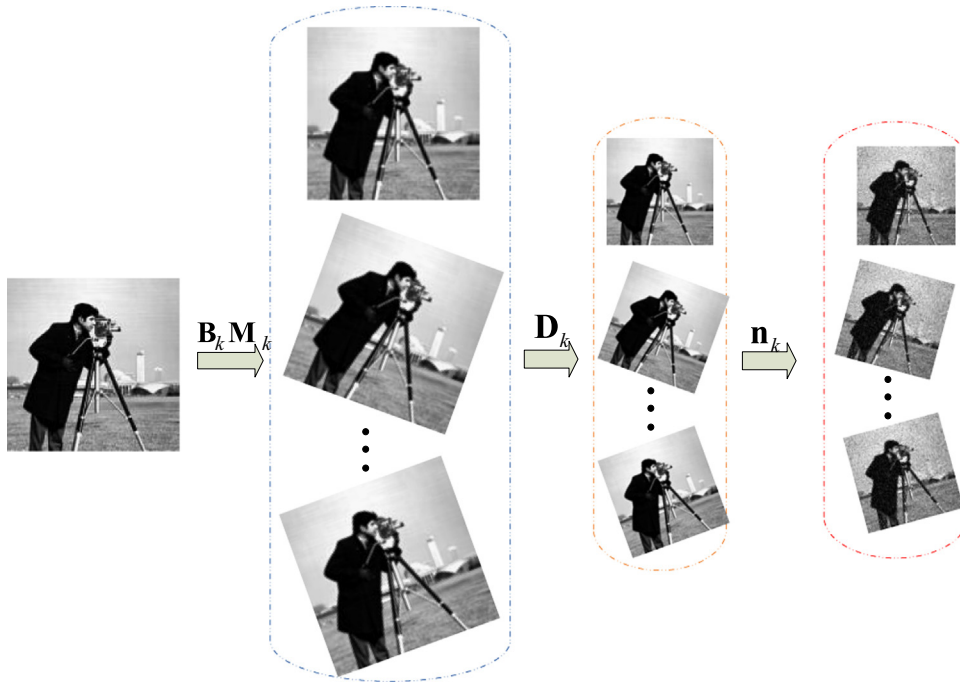


Fig. 1. The universal degradation procedure for image super-resolution.

by the downsampling factor.  $\mathbf{D}_k$ ,  $\mathbf{B}_k$ , and  $\mathbf{M}_k$  are, respectively, the downsampling, blurring, and motion operators, and  $\mathbf{n}_k$  is the additive noise. If  $\mathbf{D}_k$  and  $\mathbf{M}_k$  are excluded, it is a model for image restoration dealing with problems with only noise and blurring.

The standard regularized minimizing function usually consists of a data fidelity term describing the model error, and a regularization to constrain the model to achieve a robust solution, which is often described as [12,16,17]

$$L(\mathbf{z}) = \sum_{k=1}^K \|\mathbf{y}_k - \mathbf{D}_k \mathbf{B}_k \mathbf{M}_k \mathbf{z}\|_p^p + \lambda \mathcal{Y}(\mathbf{z}) \quad (2)$$

In (2),  $K$  represents the number of low-resolution (LR) images.  $\mathcal{Y}(\mathbf{z})$  is the regularization, which is generally chosen from Tikhonov [18], Huber–Markov random field (HMRF) [19], or total variation (TV) family [12,15,20], and  $\lambda$  is the regularized parameter which controls the tradeoff between the two terms. For the data fidelity term, the  $L_2$  norm is widely used, but it only performs well for model errors satisfying a traditional Gaussian distribution [21]. It has been proved that the  $L_1$  norm is more appropriate for impulse noise and motion outliers in image inverse problems. The reason for the robustness of  $L_1$  when handling impulse errors is based on the fact that the  $L_2$  model results in a pixel-wise mean, while the  $L_1$  model results in a pixel-wise median of all the measurements after motion compensation [15,16,22].

In the image processing field, Gaussian-type noise is the most commonly assumed because the noise generated in image acquisition usually satisfies a Gaussian distribution. However, in many applications, practical systems suffer from impulse noise/outliers, which are typically caused by malfunctioning arrays in camera sensors, faulty memory locations in hardware, or transmission in a noisy

channel [23,24]. In the image super-resolution problem, motion outliers should be specially considered because some pixels in one frame may be unobservable in the other frames [25–27]. Considering the complicated degradation of images, as with mixed noise and motion outliers, both the  $L_1$  and  $L_2$  models have their own advantages and disadvantages. Therefore, some researchers have tried to combine the advantages of the  $L_1$  and  $L_2$  norms for the fidelity [28–30]. However, the combination of  $L_1$  and  $L_2$  may result in new challenges. The hybrid-norm problem is not a standard linear problem to solve, so an efficient optimization method should be considered. In addition, the reconstruction capability of the regularized model hinges on the selection of  $\lambda$ , and different norm constraints should correspond to different weights for the tradeoff between the fidelity and the regularization. The traditional methods usually tune the weight for the hybrid norm manually, which is time consuming [31]; thus, adaptive weight estimation is an issue worth considering.

In order to deal with super-resolution with mixed noise and/or motion outliers, we propose a variational model employing a regularized framework with a locally adaptive fidelity norm. Specifically, different norm values in the data fidelity for different pixel locations are determined according to the detection results for the impulse noise and motion outliers. The  $L_1$  norm is employed for pixels with impulse noise and motion outliers, and the  $L_2$  norm is used for the other pixels. To balance the difference in the constraint strength between the  $L_1$  norm and the  $L_2$  norm, a strategy to adaptively estimate the weighted parameter is put forward.

The remainder of this paper is organized as followed. We introduce the adaptive model construction and optimization in Section 2. The norm selection is described in

Section 2.1, in which detection for impulse noise and motion outliers is presented separately. The solving strategy and the method of adaptively determining the weight for the norm-adaptive data fidelity term are given in Section 2.2. We present the experiments for super-resolution under mixed noise conditions, including real video sequence images with moving objects, in Section 3, along with a discussion of the comparative results and parameters. Section 4 is the conclusion.

## 2. The locally adaptive $L_1 - L_2$ super-resolution method

As mentioned before, the model in (2) with  $p=2$  is usually robust for the Gaussian noise case, while  $p=1$  is suitable for impulse error and/or outliers. Due to the complicated imaging process, there may be mixed noise (mainly Gaussian plus impulse noise) [29,31–34] and moving objects, which may lead to outliers in the image sequences [25–27]. To address these problems, we employ an adaptive  $L_1 - L_2$  norm framework. Driven by the detection map of the impulse noise and motion outliers, we employ different  $p$  to handle super-resolution problems. Moreover, corresponding to the different local norm constraints, different regularization parameters should also be applied. Taking these factors into account, the model can be rewritten as

$$L(\mathbf{z}) = \sum_{k=1}^K [w_k \cdot \|\mathbf{C}_k(\mathbf{y}_k - \mathbf{D}_k \mathbf{B}_k \mathbf{M}_k \mathbf{z})\|_1 + \|\tilde{\mathbf{C}}_k(\mathbf{y}_k - \mathbf{D}_k \mathbf{B}_k \mathbf{M}_k \mathbf{z})\|_2^2] + \lambda \gamma(\mathbf{z}) \quad (3)$$

In (3),  $\mathbf{C}_k$  is a diagonal matrix with the non-zero elements if the corresponding pixel belongs to the impulse noise or motion outliers in the  $k$ th frame, and  $\tilde{\mathbf{C}}_k = \mathbf{I} - \mathbf{C}_k$ ,

with  $\mathbf{I}$  being the identity matrix.  $w_k$  represents a weight for the fidelity to balance the constraint strength between the  $L_1$  and the  $L_2$  norm. The main task of our work is to adaptively determine  $\mathbf{C}_k$  and  $\tilde{\mathbf{C}}_k$ , while simultaneously estimating  $w_k$ .

### 2.1. Adaptive norm selection

In this section, we introduce the methods for selecting the norm for detection under mixed noise with Gaussian plus impulse noise (Section 2.1.1) and noise with motion outliers (Section 2.1.2). The flowchart for the adaptive norm selection is shown in Fig. 2. Impulse noise and motion outliers are detected separately, and the locally adaptive  $L_1 - L_2$  norm is selected based on the detection results. We use  $L_1$  to handle the impulse noise pixels and motion outliers (the light pixels in the detection results in Fig. 2) and we adopt  $L_2$  for the other pixels.

#### 2.1.1. For mixed Gaussian/impulse noise

For images corrupted by mixed noise (Gaussian and impulse), we can revise the degradation process, as shown in Fig. 3. Based on a statistical viewpoint, we believe that the noise distribution can be described by a probability distribution. Gaussian noise has a quadratic Gaussian distribution, and impulse noise is likely to satisfy a Laplacian distribution [28].

According to the corruption procedure, as shown in Fig. 3 [35], we suppose the images are corrupted by Gaussian noise with a mean value 0 and standard deviation  $\sigma$ , and impulse noise with noise density  $s$ . We denote  $y_0(i, j)$  as a noiseless pixel of image  $\mathbf{y}_0$  with size  $n_1 \times n_2$  at pixel location  $(i, j)$ , for each pixel  $y(i, j)$  with Gaussian or

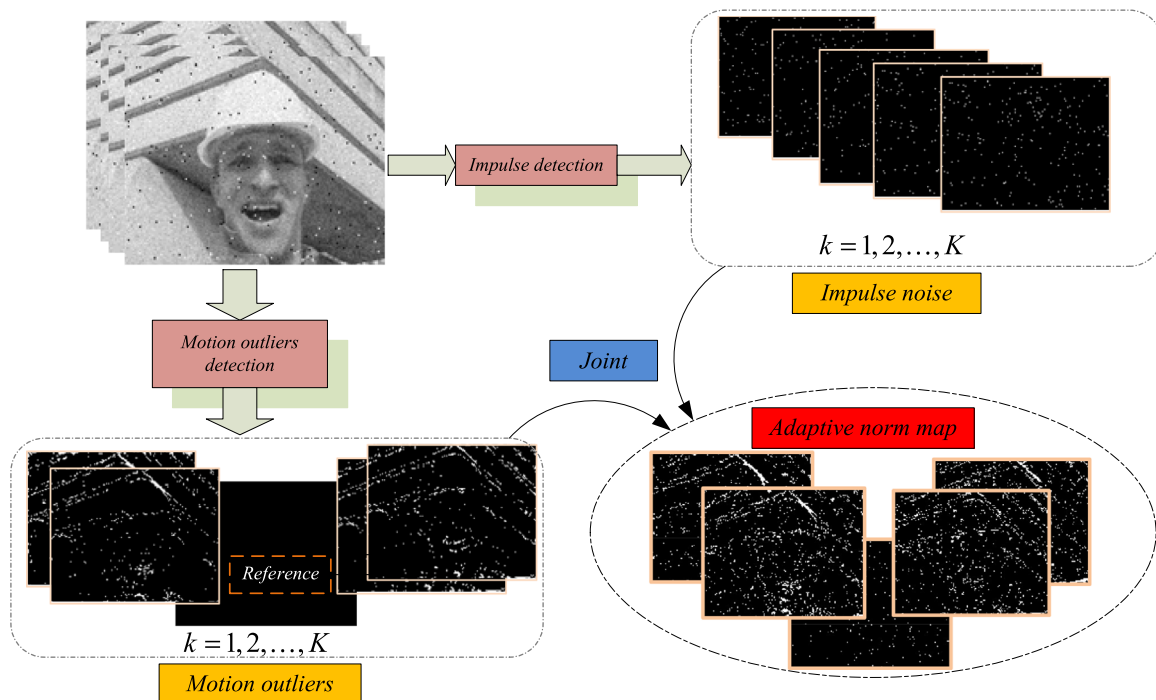


Fig. 2. The procedure used to determine the adaptive norm for the data fidelity term.

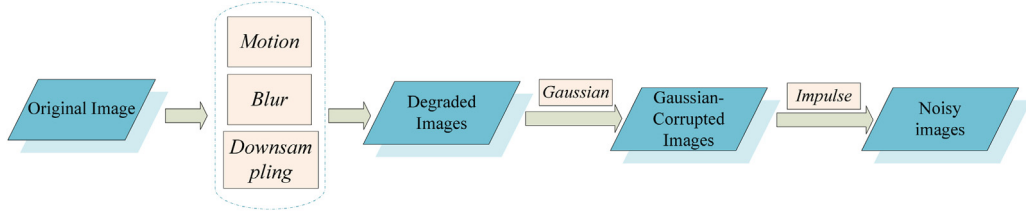


Fig. 3. Degradation procedure for mixed noise.

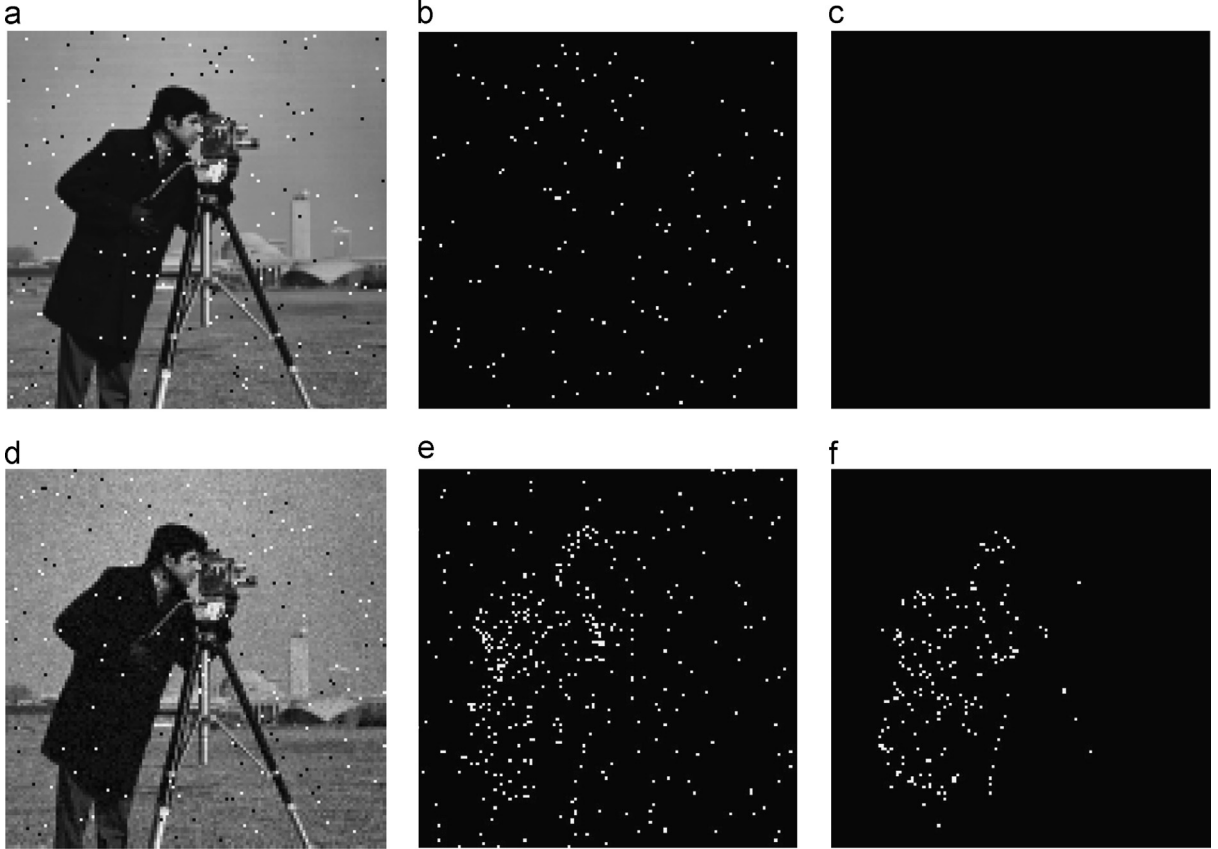


Fig. 4. Detection results for the *Cameraman* image. (a) Impulse noisy image, (b) detection results, (c) detection error, (d) mixed noisy image, (e) detection results, and (f) detection error.

impulse noise, which can be modeled by

$$y(i,j) = \begin{cases} I(i,j) & \text{with prob. } s \\ y_0(i,j) + n(i,j) & \text{with prob. } 1-s \end{cases} \quad (4)$$

where  $n(i,j)$  means the gray level of noise for each pixel satisfying a Gaussian distribution, and  $I(i,j)$  is decided by the type of impulse noise. For random-valued impulse noise, it means a gray level of identically and uniformly distributed random numbers between  $[I_{\min}, I_{\max}]$ , which means the dynamic range of an image, while for salt and pepper noise,  $I(i,j)$  can be expressed as

$$I(i,j) = \begin{cases} I_{\min} & \text{with prob. } s/2 \\ I_{\max} & \text{with prob. } s/2 \end{cases} \quad (5)$$

As Fig. 2 shows, the adaptive norm selection method is mainly based on the detection of pixels contaminated by impulse noise. A simple but efficient method dealing with impulse noise [36] is employed here. The feature of the digital image is usually local correlation, and the feature of the impulse noise is usually located near one of the two ends of the image's maximum and minimum gray values. Based on this principle, the detection method achieves a good performance.

We give detection results for the *Cameraman* image under different noise types below. In Fig. 4, (c) and (f) represent the detection error map corresponding to (a) and (d), in which the light pixels are the wrongly detected impulse noise pixels. With mixed noise, there is a certain error in the detection results for the location of the impulse noise. However, it can be analyzed that all the

impulse noise pixels are detected correctly, although some other pixels polluted by Gaussian noise are wrongly detected as impulse noise. Fortunately, our experiments show that the reconstruction based on this detection was not significantly affected.

### 2.1.2. For motion outliers

Multi-frame super-resolution has the advantage over other techniques that it can make use of the redundant information between LR image sequences with a relative sub-pixel motion. As presented above, relative shift and translation may exist between LR images, so motion estimation/registration plays a significant role in super-resolution reconstruction [37]. Methods for attaining the sub-pixel motion generally apply a parametric or nonparametric motion model [10,12,38] to get the motion vector between the sequences. However, the registration error within the complex model, and the discontinuous pixels caused by moving targets, will influence the reconstruction performance. In our reconstruction model, we take advantage of  $L_1$  when dealing with the discontinuous pixels caused by moving objects and the detected registration errors, and we accordingly adopt an adaptive norm to take both noise and outliers into consideration.

After acquiring the motion vector  $\mathbf{m}$  between the observed frame  $\mathbf{y}_k$  and the referenced frame  $\mathbf{y}_l$ ,  $\mathbf{y}_k^{(l,m)}$ , which is the estimated frame of  $\mathbf{y}_k$  from frame  $l$ , can be

obtained using  $\mathbf{m}$ . In accordance with the motion estimation results, we can detect the outliers using a threshold for the difference of the corresponding pixel value between the unreferenced frame and the referenced frame after registration. To reduce the detection error at the objects' edges, we include spatial gradient information to spatially adaptively detect the existing outliers:

$$|\mathbf{y}_k(i,j) - \mathbf{y}_k^{(l,m)}(i,j)| < T \times S(i,j) \quad (6)$$

Here,  $S(i,j)$  represents the structure tensor matrix [39] of  $\mathbf{y}_k$  with a size of  $n_1 \times n_2$ , which can reflect the complexity of the texture for the image at location  $(i,j)$ , and  $T$  is the control threshold. To suppress the effect of noise as far as possible, a smoothing filter process and spatial clustering are enforced on the calculated structure tensor [40] before it is used for judgment. This means that after the structure tensor matrix is calculated, it is filtered and clustered with  $K$ -means [41] to get the matrix  $\mathbf{S}$  in (6). If the absolute difference between the pixel values does not satisfy the equation, we consider that the pixel should be classified as an outlier, and we handle it with the  $L_1$  norm. The detection results for the *Foreman* image are shown in Fig. 5, with the outliers displayed as dark pixels, in which (a)–(c) are the results only considering a threshold, while (d)–(f) represent the detection map, including the image's local spatial information. We can conclude that with a clustered

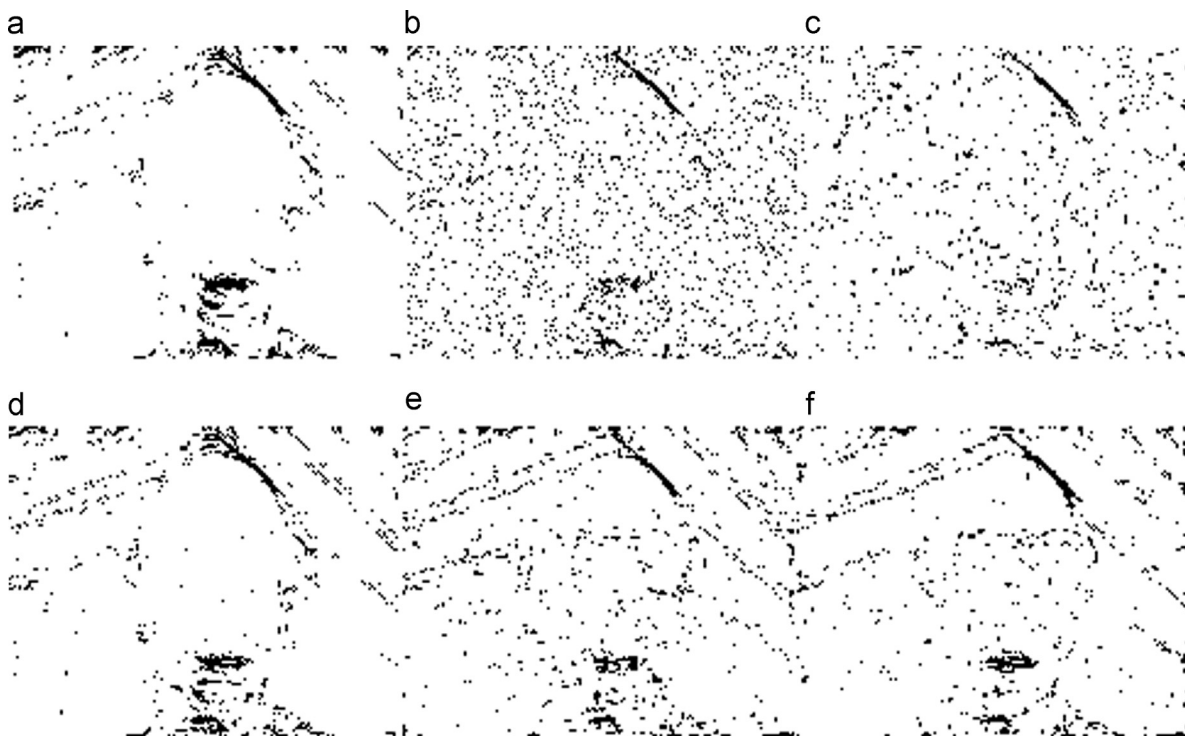


Fig. 5. Motion outlier detection results for the *Foreman* image. (a) Noiseless ( $T=10$ ), (b) Gaussian noise ( $T=20$ ), (c) mixed noise ( $T=30$ ), (d) noiseless ( $T=0.2$ ), (e) Gaussian noise ( $T=0.2$ ), and (f) mixed noise ( $T=0.3$ ).

structure tensor as the spatial information, the motion outlier detection has relatively stable results, even with noise.

By detecting the impulse noise and the motion outliers, as presented before, we can divide each LR image into two parts. The detection result can be stored as a mask matrix  $Q_k$  with size  $n_1 \times n_2$ , with a labeled value of 1 where pixels are detected as impulse noise/motion outliers, while the other values are 0. The norm maps  $C_k$  and  $\tilde{C}_k$  can be accordingly determined as the diagonal weight matrix with size  $n_1 n_2 \times n_1 n_2$ . Set  $i = 1, 2, \dots, n_1, j = 1, 2, \dots, n_2$ , and  $C_k$  can be

given as

$$C_k(l, l) = \begin{cases} 1 & \text{if } Q_k(i, j) = 1 \\ 0 & \text{if } Q_k(i, j) = 0 \end{cases} \quad l = i + (j - 1) \times n_1 \quad (7)$$

### 2.2. Adaptive weight estimation and model optimization

The selection of the regularization  $Y(z)$  is a pivotal task for the reconstruction. However, the proposed model has the advantage of being able to flexibly add a prior constraint. In this study, our main purpose

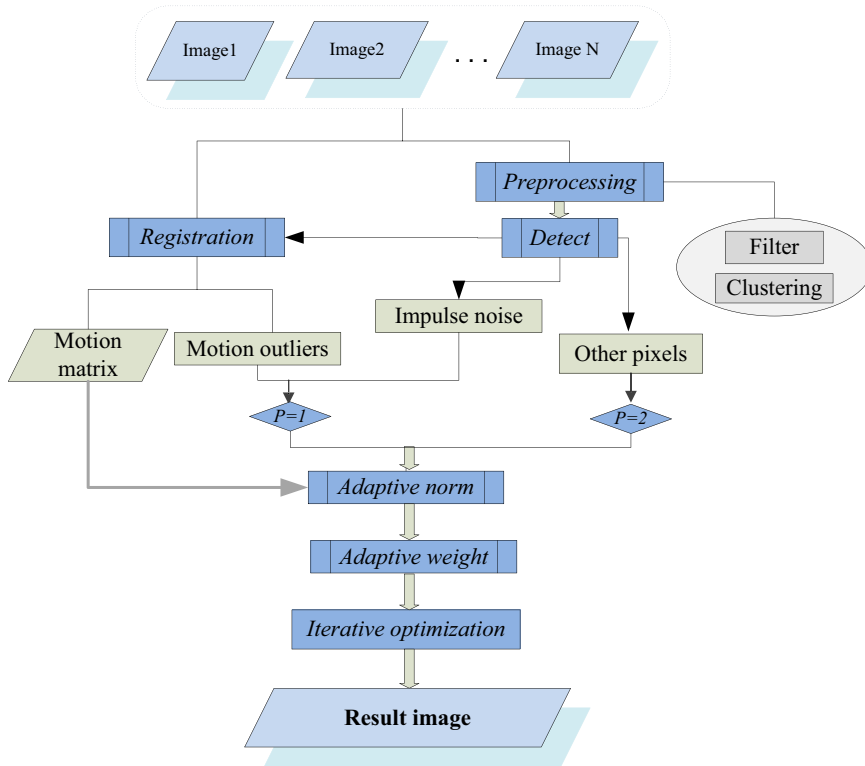


Fig. 6. Diagram of the whole super-resolution procedure flow.

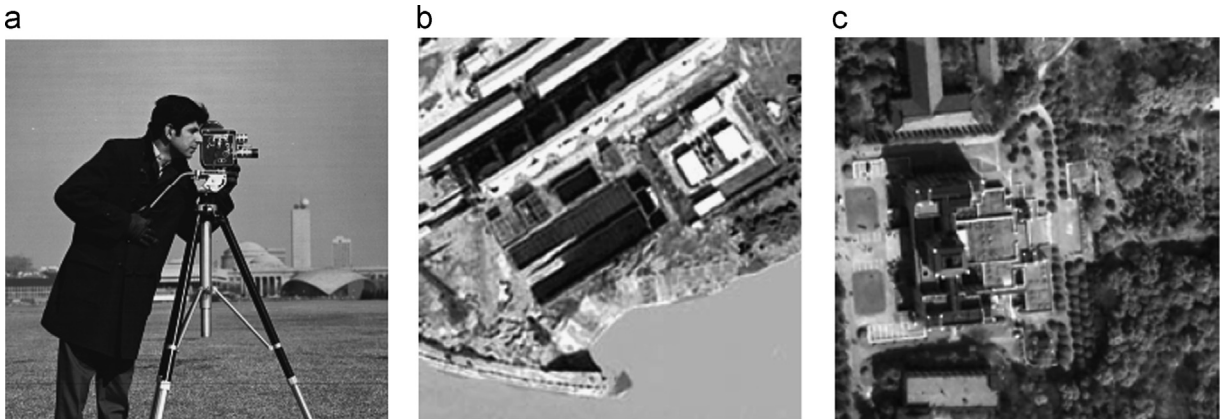


Fig. 7. Original images for the mixed noise super-resolution experiments. (a) Cameraman, (b) aerial, and (c) remote sensing.

is to test the performance of an adaptive norm for the data fidelity term, so we choose TV regularization [12] as the prior due to its performance in suppressing noise and preserving edges for image reconstruction. Some improved regularizations, such as spatially adaptive TV [20,40,42,43], higher-order TV [44,45], and nonlocal based regularization [46], could also be chosen.

2.2.1. The iteratively reweighted norm

As mentioned before, the general minimization expression based on TV can be represented as

$$L(\mathbf{z}) = \sum_{k=1}^K [w_k \cdot \|C_k(\mathbf{y}_k - \mathbf{A}_k \mathbf{z})\|_1 + |\tilde{C}_k(\mathbf{y}_k - \mathbf{A}_k \mathbf{z})|_2^2] + \lambda \|\sqrt{(\nabla^x \mathbf{z})^2 + (\nabla^y \mathbf{z})^2} + \beta\|_q^q \quad (8)$$

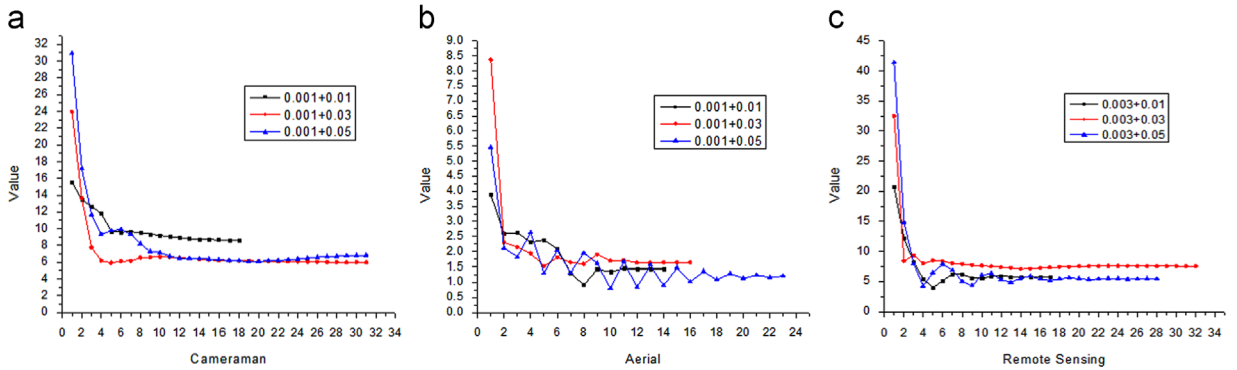


Fig. 8. The average weights of different images under different noise cases for super-resolution.

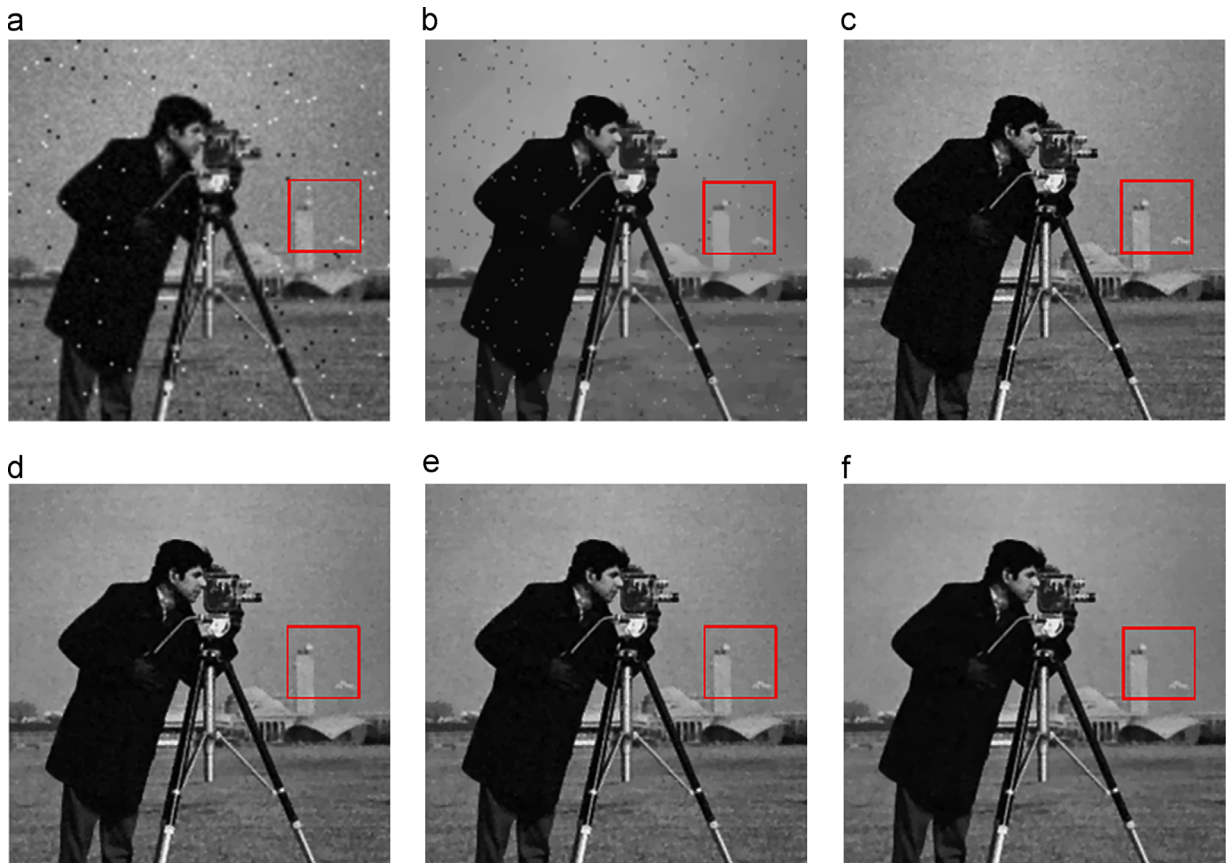


Fig. 9. Super-resolution results for the corrupted *Cameraman* image with “0.001+0.01”. (a) LR image, (b) result of  $L_2$ , (c) result of  $L_1$ , (d) result of M-estimator, (e) result of the optimal global norm, and (f) result of the proposed method. (For interpretation of the references to color in this figure caption, the reader is referred to the web version of this paper.)

where to facilitate the expression, we set  $\mathbf{A}_k = \mathbf{D}_k \mathbf{B}_k \mathbf{M}_k$ .  $\nabla^x$  and  $\nabla^y$  are linear operators corresponding to the horizontal and vertical first-order differences, and  $\beta$  is a small positive parameter which ensures differentiability. For pixel  $(i, j)$ , for example, we have  $\nabla_{ij}^x \mathbf{z} = z(i, j+1) - z(i, j)$  and  $\nabla_{ij}^y \mathbf{z} = z(i+1, j) - z(i, j)$ . Here, we set  $q=1$ , which indicates the general TV model:

$$L(\mathbf{z}) = \sum_{k=1}^K [w_k \cdot \|\mathbf{C}_k(\mathbf{y}_k - \mathbf{A}_k \mathbf{z})\|_1 + \|\tilde{\mathbf{C}}_k(\mathbf{y}_k - \mathbf{A}_k \mathbf{z})\|_2^2] + \lambda \sqrt{(\nabla^x \mathbf{z})^2 + (\nabla^y \mathbf{z})^2} + \beta \quad (9)$$

For this hybrid-norm model, it has difficulty in employing conventional numerical methods for quadratic problems like the  $L_2$  norm directly, due to the nonlinearity. Numerous efforts [47–51] have been made to solve nonlinear inverse problems. In this paper, we employ iteratively reweighted norm (IRN) as the optimization method for the multi-frame super-resolution model in (9) due to its effectiveness and simplicity [50]. It is noted that despite IRN adopted in this paper, some other optimization algorithms such as proximal splitting methods including parallel proximal algorithm (PPXA) [47] and alternating direction method of multipliers (ADMM) [47,49] are also capable of handling nonlinear inverse problems like (9). The iteratively reweighted norm (IRN) [50] is an efficient smooth approximation algorithm for solving the TV/ $L_p$  problem,

by representing the generalized  $L_p$  norm with the equivalent weighted  $L_2$  norm, and thus we obtain a linearized expression suitable for the quadratic optimization methods.

Specifically, in order to replace the  $L_p$  with the  $L_2$  norm, we denote the quadratic expression as

$$L^{(r+1)}(\mathbf{z}) = \sum_{k=1}^K [w_k^{(r)} \cdot \|\Omega_{(r)}^{1/2} \mathbf{C}_k(\mathbf{y}_k - \mathbf{A}_k \mathbf{z})\|_2^2 + \|\tilde{\mathbf{C}}_k(\mathbf{y}_k - \mathbf{A}_k \mathbf{z})\|_2^2] + \lambda \sqrt{(\nabla^x \mathbf{z})^2 + (\nabla^y \mathbf{z})^2} + \beta \quad (10)$$

where  $w_k^{(r)}$  represents the weight for the  $r$ th iteration, and  $\Omega_{(r)}$  is the iteratively reweighted matrix, defined by

$$\Omega_{(r)} = \text{diag}(\tau_\xi(\mathbf{y}_k - \mathbf{A}_k \mathbf{z}_{(r)})) \quad (11)$$

where

$$\tau_\xi(x) = \begin{cases} |x|^{p-2} & \text{iff } |x| > \xi \\ \xi^{p-2} & \text{else} \end{cases} \quad (12)$$

where  $\xi$  is a small positive scalar to avoid the possibility of division by zero, which is fixed as  $10^{-5}$  in this paper. In addition, we employ lagged diffusivity fixed point iteration (LDFPI) [52] for the TV linearization. After linearization, the model can be solved by PCG, which is a desirable optimization solution for inverse problems [12].

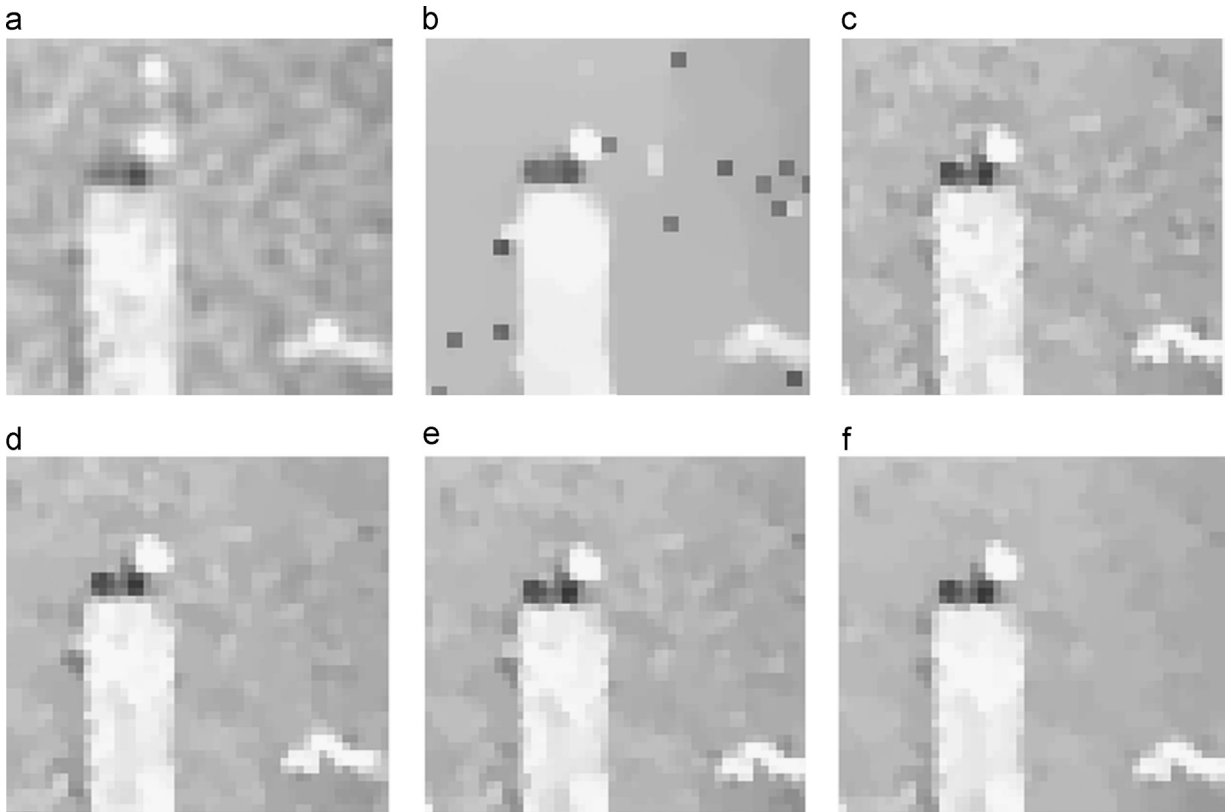


Fig. 10. The corresponding cropped images of Fig. 9.

### 2.2.2. Adaptive weight estimation

As discussed before, the locally adaptive norm algorithm in our model has a hybrid norm with either  $L_1$  or  $L_2$  for each pixel. In general, we usually need a smaller regularization parameter if  $L_1$  is adopted as the data fidelity term in (2). Therefore, we introduce a weight  $w_k$  for the fidelity to balance the difference in constraint strength between the two items. However, complex parameter selection is always a headache. We attempt to determine  $w_k$  for the data fidelity term in our model (9) adaptively. In later experiments (Section 3), the effectiveness of the adaptive parameter selection strategy is verified.

In the previous part (Section 2.2.1), we used an IRN method to achieve conversion from the  $L_1$  to the  $L_2$  norm. Only considering the part of the  $L_1$  norm, we denote

$$F_k(\mathbf{z}) = w_k^{(r)} \|\Omega_{(r)}^{1/2} \mathbf{C}_k(\mathbf{y}_k - \mathbf{A}_k \mathbf{z})\|_2^2 \quad (13)$$

For this part,  $\lambda$  is appropriate if  $L_2$  is used to constrain  $\mathbf{C}_k(\mathbf{y}_k - \mathbf{A}_k \mathbf{z})$ . To make this suit  $\|\mathbf{C}_k(\mathbf{y}_k - \mathbf{A}_k \mathbf{z})\|_1$ , we need to consider the proportional relationship between the different norm constraints for the same item, and thus determine the weight. To simplify the calculation, we make use of the IRN's conversion matrix to obtain the proportion, instead of the exact relationship. This can be analyzed if  $L_2$  is adopted for the constraint, where we can regard all

the non-zero elements of the iteratively reweighted matrix as 1, and  $\Omega_{(r)}$  is the weighted matrix obtaining the  $L_2$  norm from the original  $L_1$  norm term. Based on this, we can use the number of non-zero pixels belonging to the  $\mathbf{C}_k$  set as  $N_C$ , and the sum of the diagonal matrix  $\Omega_{(r)}$  for the weight estimation. The weight  $w_k^{(r)}$  we require is calculated by

$$w_k^{(r)} = N_C / \Sigma \Omega_{(r)} \quad (14)$$

Super-resolution with noise/outliers can be generalized into the adaptive norm framework, as shown in Fig. 6. The experiments in Section 3 demonstrate that this is a universal model that is able to handle image super-resolution with single or mixed noise and/or motion outliers. Additionally, the adaptive strategy is able to obtain results that are similar to or equivalent to the manual methods, which demonstrates its robustness in application.

### 3. Experiments

The experiments consist of two parts, to test the effectiveness of the proposed model in handling super-resolution for images with mixed noise and/or motion outliers. In the first part (Section 3.1), three commonly used images with different resources, and contaminated by different levels of mixed noise, are chosen as the test

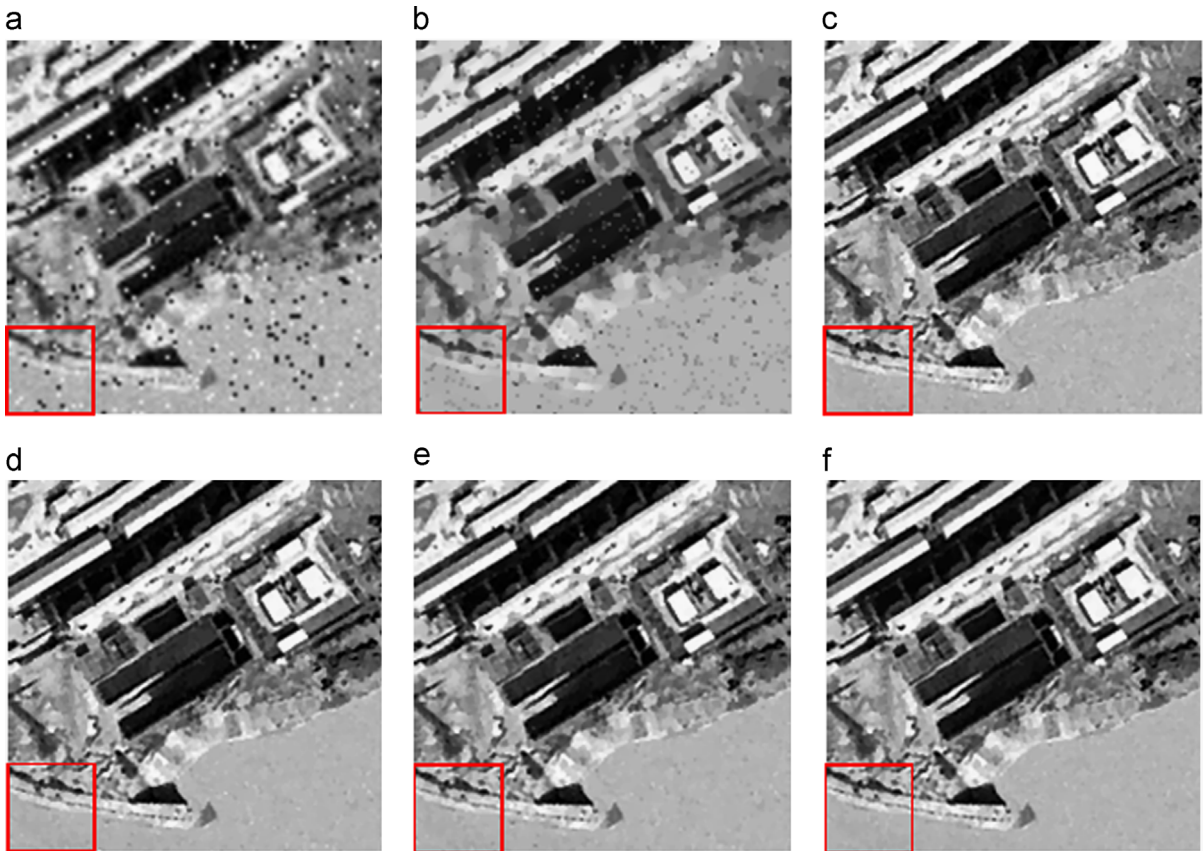


**Fig. 11.** Super-resolution results for the corrupted Aerial image with “0.001+0.05”. (a) LR image, (b) result of  $L_2$ , (c) result of  $L_1$ , (d) result of M-estimator, (e) result of the optimal global norm, and (f) result of the proposed method. (For interpretation of the references to color in this figure caption, the reader is referred to the web version of this paper.)

images. The experiments in this part are mainly designed to test the effectiveness of the model in suppressing mixed noise during super-resolution. The experiments in the second part are for video frame images. There are moving objects in the video frames we chose, so as to test the performance of the model for motion outliers plus noise in both synthetic and real cases.

### 3.1. Super-resolution under mixed noise

The three images in Fig. 7 are chosen to test the super-resolution algorithm with mixed noise. Among them, the *Cameraman* image has a size of 256\*256, and the size for the other two is 200\*200. The synthetic experiments are first implemented. The LR images are acquired from a single-frame HR image with a given sub-pixel motion between them. In this set of experiments, sub-pixel shifts of (0, 0), (0.5, 0), (0, 0.5), (0.5, 0.5) are implemented, and we assume that the motions are accurately captured and estimated. The noise in the images is simulated as (4). The LR images are corrupted by zero-mean Gaussian noise with a different variation  $\sigma^2$  (after normalization), and salt and pepper noise with noise ratio  $s$ .

We give the curves in Fig. 8 displaying the average weights for the frames used in the reconstruction. Figs. 9–14 show the corresponding results visually and subjectively. Here, we give the results of the three experiments to verify the efficacy of the proposed method when compared with the other popular variational frameworks. The adaptive super-

resolution method is compared with fixed  $L_1$  norm and  $L_2$  norm methods. We notice that neither  $L_1$  nor  $L_2$  is optimal when there is mixed noise [28]. To confirm the advantage of proposed method more adequately, we manually selected the optimal norms as decimal values in the interval of [1,2], and we use these results for comparison in the experiments for mixed noise [50]. The results of the adaptive method based on M-estimator in [30] are also included to further demonstrate the effectiveness of the proposed model. This method proposed by Zeng et al. forms a fidelity term model by an adaptive strategy depending on the accuracies of the estimated LR image observation models, and is thus able to deal with impulse noise and registration errors. It is worth mentioning that only different adaptive data fidelity terms are adopted in the experiments, to allow a fair comparison. In all the experiments, we tune the parameters of our model, as well as the methods for comparison, to get the appropriate results with the highest peak signal-to-noise ratio (PSNR). The quantitative results are given in Tables 1–3. Both the PSNR and the structural similarity index (SSIM) [53,54] are used to measure the quality of the results.

In the tables, the noise case is expressed by “ $\sigma^2+s$ ”. “Global” means the manually optimal global norm for the fidelity [50]. For the case with pure Gaussian noise,  $L_2$  is the optimal global norm; while for images with pure impulse noise,  $L_1$  is suitable. For a more detailed analysis of the results, the methods are compared under two conditions. “Manual” indicates that we adopt different parameters for the different norms by tuning the parameters

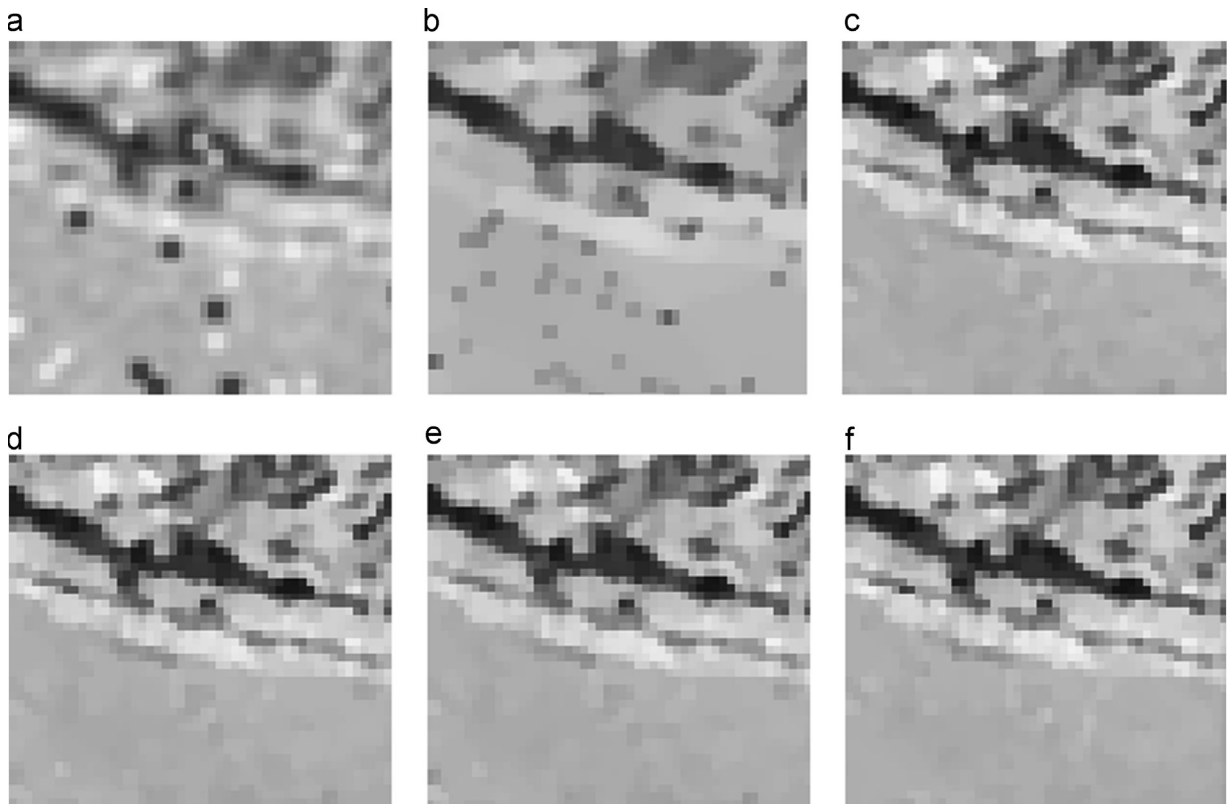
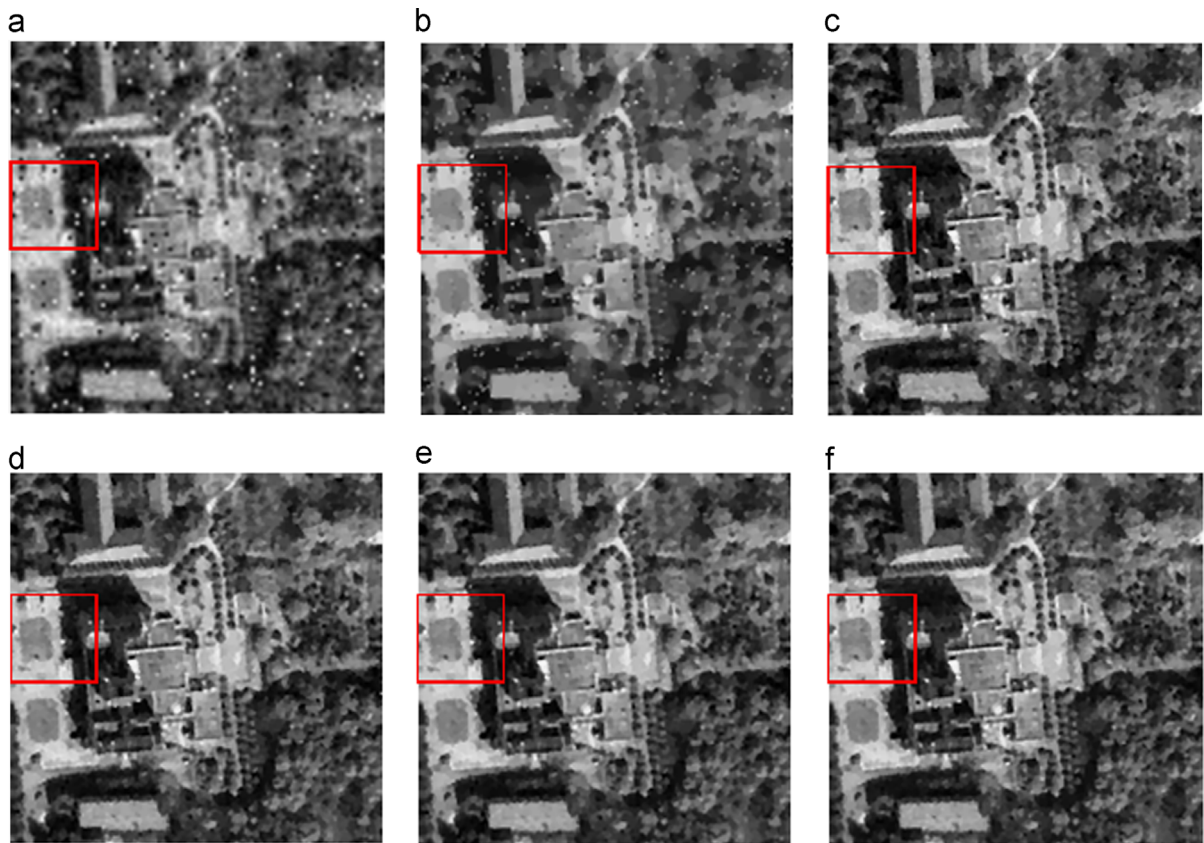


Fig. 12. The corresponding cropped images of Fig. 11.



**Fig. 13.** Super-resolution results for the corrupted *Remote Sensing* image with “0.003+0.03”. (a) LR image, (b) result of  $L_2$ , (c) result of  $L_1$ , (d) result of M-estimator, (e) result of the optimal global norm, and (f) result of the proposed method. (For interpretation of the references to color in this figure caption, the reader is referred to the web version of this paper.)

manually, while “Adaptive” represents the results for the adaptive weight estimation mentioned in Section 2.2.2. It can be clearly observed that the proposed method achieves the highest PSNR and SSIM values under all situations, compared with the other methods.

Specifically, when the image is contaminated with mixed noise,  $L_1$  is better than  $L_2$  because  $L_2$  cannot completely remove the specks while preserving the texture. Comparatively, the  $L_1$  norm is not as good at handling Gaussian-type errors, and has low efficiency. However, the optimal global results show that neither  $L_1$  nor  $L_2$  is optimal. The global methods select a decimal global norm belonging to [1,2] to constrain the data fidelity term, and get better results than the single  $L_1$  and  $L_2$  norms. When the images are mainly dominated by impulse noise, the optimal norm is approximate to  $L_1$ , while in the case of the images being contaminated by “0.001+0.05” (Gaussian noise with  $\sigma^2 = 0.001$  and impulse noise with  $s = 0.05$ ), the optimal global norm is the same as  $L_1$ . From the super-resolution results presented in the experiments, the proposed method has an overwhelming advantage over the other methods, and shows a significant improvement over the global method. In general, although there are different degrees of volatility, the results show that the adaptive weight estimation method has similar results to the manual methods, thus confirm the accuracy of the parameter estimation through a considerable amount of experiments. It can be seen in Fig. 8 that the

values of the weights change with the iteration, and they vary according to the content of the images.

In Figs. 10, 12 and 14, the cropped regions correspond to the rectangular area in Figs. 9, 11 and 13, respectively. Consistent with the theoretical assumptions, neither the  $L_1$  norm nor the  $L_2$  norm could get ideal results. For example, in Fig. 10, (b) represents the result with  $L_2$ . Its weakness to impulse noise means that it has difficulty in achieving a balance between removing noise and preserving the detailed texture. Furthermore, in Fig. 10(c), the  $L_1$  norm performs well in removing the speckle noise, but some Gaussian-distributed noise remains. The results in Fig. 10 (d) and (e) indicate that better results can be acquired with the global norm and M-estimator. The results with the M-estimator [30] show a better performance than the global norm when impulse noise plays the dominant role. We can see apparent visual improvements with the proposed method in the *Cameraman* and *Aerial* experiments. Overall, the pixel-based adaptive norm has the best super-resolution results, with the noise being suppressed and the texture preserved. For the *Remote Sensing* image, the more complex textures make the difference in visual effects hard to recognize. However, we can see that detailed texture and information are better preserved in Fig. 14(e) than Fig. 14(c) and (d). Meanwhile, the adaptive weight estimation shows its effectiveness and stability in the experiments.

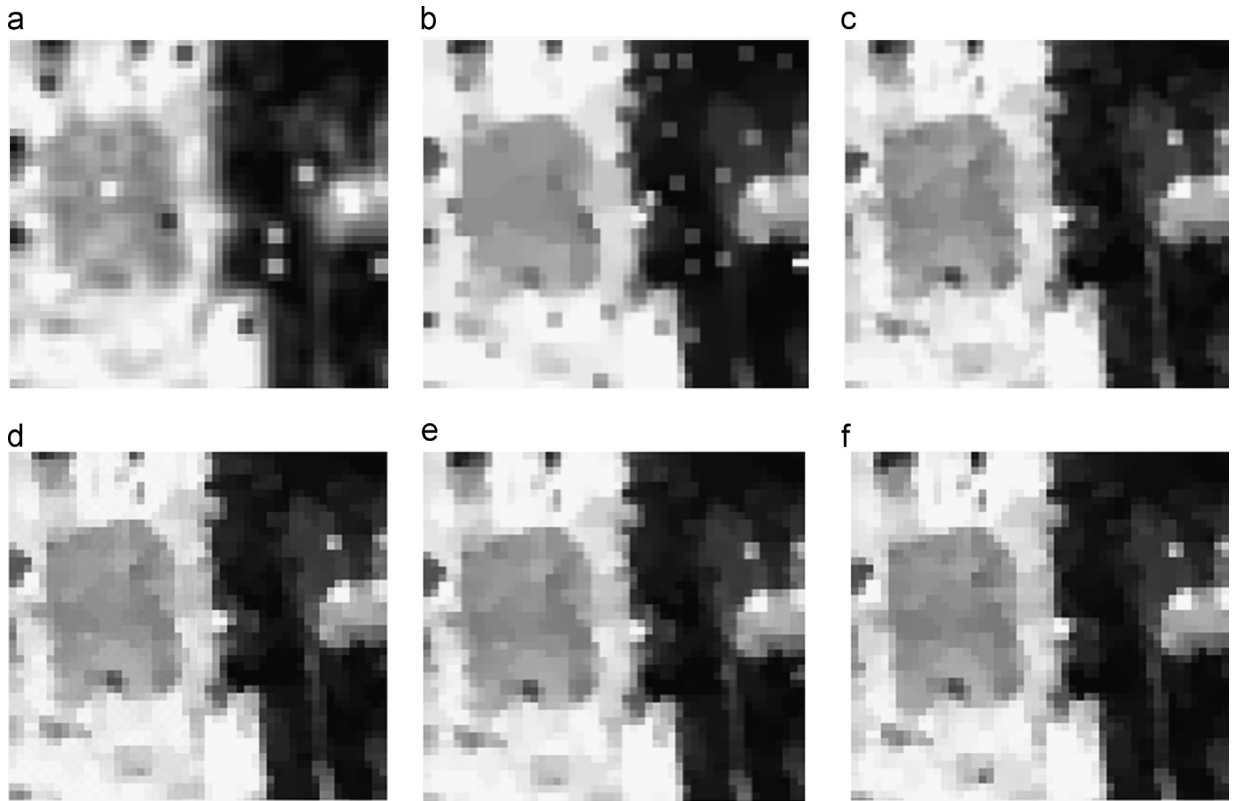


Fig. 14. The corresponding cropped images of Fig. 13.

Table 1

Quantitative evaluation results of the *Cameraman* image experiments.

Noise ( $\sigma^2 + s$ )	L2	L1	M-estimator	Global	Manual	Adaptive
0.001 + 0.01						
PSNR	26.276	29.563	29.803	29.908	30.582	30.414
SSIM	0.751	0.839	0.849	0.854	0.874	0.883
0.001 + 0.03						
PSNR	24.901	29.366	29.843	29.453	30.500	30.422
SSIM	0.712	0.832	0.856	0.824	0.871	0.872
0.001 + 0.05						
PSNR	24.333	29.167	29.431	29.167	30.419	30.254
SSIM	0.698	0.834	0.855	0.834	0.879	0.879

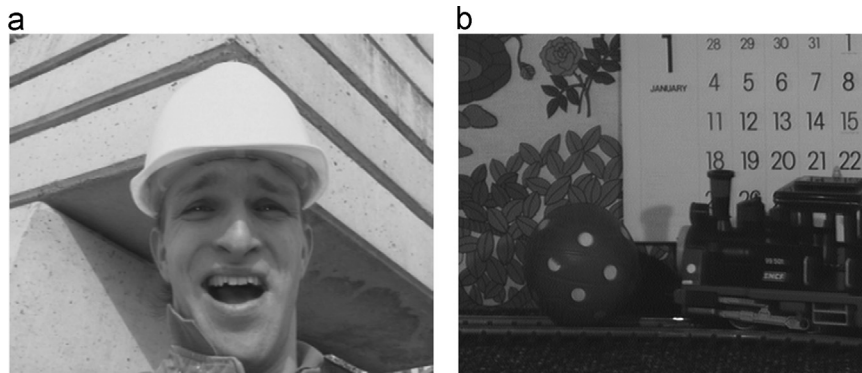
Table 2

Quantitative evaluation results of the *Aerial* image experiments.

Noise $\sigma^2 + s$	L2	L1	M-estimator	Global	Manual	Adaptive
0.001 + 0.10						
PSNR	24.088	27.548	28.274	27.920	28.503	28.364
SSIM	0.817	0.904	0.925	0.917	0.925	0.928
0.001 + 0.03						
PSNR	22.273	27.277	27.845	27.408	28.419	28.403
SSIM	0.723	0.906	0.921	0.908	0.926	0.926
0.001 + 0.05						
PSNR	21.319	27.071	27.330	27.071	28.297	28.256
SSIM	0.676	0.900	0.910	0.900	0.923	0.922

**Table 3**Quantitative evaluation results of the *Remote Sensing* image experiments.

Noise ( $\sigma^2 + s$ )	L2	L1	M-estimator	Global	Manual	Adaptive
0.003+0.01						
PSNR	23.807	24.896	25.575	25.359	25.844	25.855
SSIM	0.794	0.838	0.860	0.855	0.866	0.866
0.003+0.03						
PSNR	22.113	24.747	25.354	25.020	25.836	25.803
SSIM	0.699	0.835	0.855	0.843	0.867	0.866
0.003+0.05						
PSNR	21.569	24.598	25.085	24.631	25.714	25.699
SSIM	0.649	0.829	0.846	0.831	0.863	0.862

**Fig. 15.** Original frames of the video sequences. (a) The 24th frame of the *Foreman* sequence; and (b) the 37th frame of the *Mobile and Calendar* sequence.

### 3.2. Super-resolution with motion outliers

To verify the effectiveness of the proposed method on video data with outliers caused by moving objects, we undertake three sets of experiments. Two of the experiments use the *Foreman* and *Mobile and Calendar* standard uncompressed video sequences (Fig. 15). The final experiment is carried out on a real compressed video sequence called *Alpaca*.<sup>1</sup>

In the *Foreman* experiments, with an original frame size of  $320 \times 256$ , frame 24 is set as the referenced frame for the result evaluation, and frames 22, 23, 25, and 26 are used as the unreferenced frames. Compared to the *Foreman* sequence, there are more complicated motions in the *Mobile and Calendar* sequence: the background moves to the right, the calendar has vertical displacements, the train moves from right to left, and a revolving ball exists in the scene. The frame size of this sequence is  $352 \times 288$ , and five frames in all were chosen, among which frame 37 is used as the reference frame for the evaluation.

The LR images used in the super-resolution construction are obtained using the corresponding HR frames in the video, with a downsampling factor of two. Noiseless images and images with mixed noise are separately used in the experiments to verify the effectiveness of the proposed model under different conditions. It should be

noted that the motions between the LR images are unknown and needed to be estimated. In the experiments, an efficient optical flow based method [12,55] is employed for the motion estimation. After the motion estimation, outliers caused by moving objects and cameras are estimated by (6), and the threshold  $T$  is empirically chosen to be 0.1–0.3, according to the noise intensity.

Figs. 16–18 display the visual difference in the reconstruction results for the *Foreman* video sequence. Figs. 19–21 show the visual results for the *Mobile and Calendar* sequence. We can conclude from the two experiments that the  $L_2$  norm is likely to cause pseudo marks when handling outliers in image reconstruction, thus affect the quality of the results, while the  $L_1$  norm is more stable when handling registration errors, but has no advantage when dealing with Gaussian noise. The method based on the M-estimator performs well and successfully overcomes the impact of the motion outliers, to a certain degree. However, the error classification estimated by the errors' residual alone causes a serious weakness with noise. The proposed method uses the  $L_1$  norm to process the outliers caused by moving objects and the impulse noise pixels. At the same time, the  $L_2$  norm is employed for the other pixels corrupted by Gaussian noise, thereby effectively suppressing both the pseudo marks and the noise.

Tables 4 and 5 give the quantitative reconstruction results. Considering that some researchers have efficiently avoided the estimation error by excluding the pixels classified as outliers in (6) [12,56], the quantitative results for this simple method are also given. In addition, the global norm

<sup>1</sup> The *Foreman* and *Mobile and Calendar* video sequences are available at <http://media.xiph.org/video/derf/>, while the compressed *Alpaca* data can be downloaded at <http://www.ee.ucsc.edu/~milanfar>.

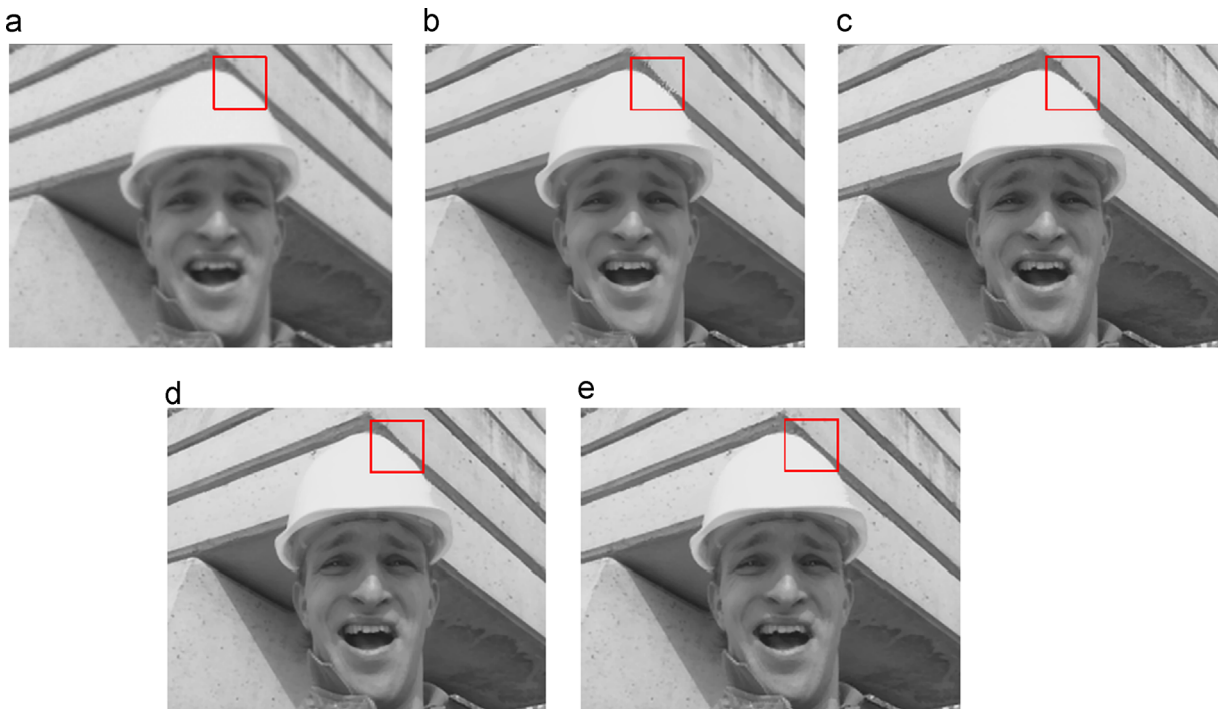


**Fig. 16.** Super-resolution results for the *Foreman* video noiseless sequence. (a) LR image, (b) result of  $L_2$ , (c) result of  $L_1$ , (d) result of M-estimator, and (e) result of the proposed method. (For interpretation of the references to color in this figure caption, the reader is referred to the web version of this paper.)

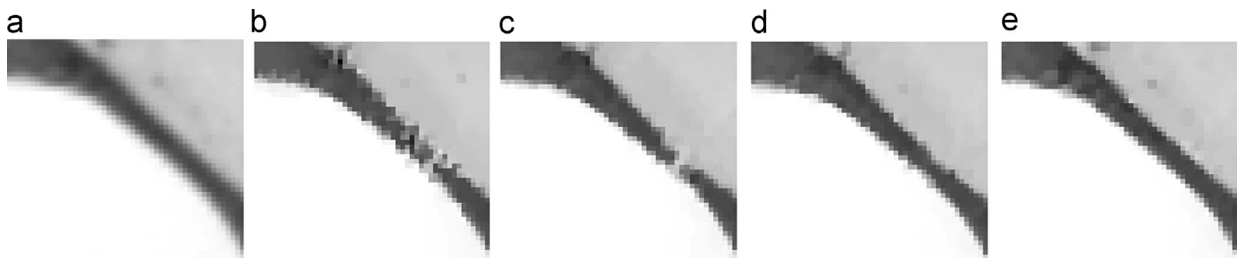


**Fig. 17.** The corresponding cropped images of Fig. 16.

method mainly concentrates on the problem of mixed noise, so the results are not included for the comparison with moving objects. “ $L_2-O$ ” and “ $L_1-O$ ” represent the corresponding methods, excluding the outliers caused by moving objects. By excluding the outliers, the  $L_2$  norm also shows a relatively stable performance. The reason for this is that it regards the super-resolution problem as an inpainting model, and thus the missing pixels can be filled using redundant information between the LR images efficiently, if the outliers are distributed discretely.

What if mixed noise and motion outliers exist at the same time? The results show that the proposed method retains an apparent advantage in this situation. It can be clearly seen that the  $L_1$  norm is more robust in handling mixed noise, and shows a significant improvement over the  $L_2$  norm. With Gaussian/impulse mixed noise, the proposed method shows a considerable improvement over

the other methods, and it succeeds in preserving the profile of the numbers in the calendar in Fig. 21. To sum up, the proposed method shows a robust performance in removing noise and maintaining clear edge information, even though there are motion outliers in the video sequence. The proposed method is a universal and general framework that can be used to handle the super-resolution problem with various noise cases, and it shows clear advantages when compared to the other methods with mixed noise.

The final experiment is for a real video sequence called *Alpaca*, which is composed of 55 compressed grayscale frames of size  $32 \times 70$ . The sequence is captured with a commercial webcam (3Com, Model no. 3718). In this sequence, in addition to the global motion created by camera shake, there is a more complicated motion model, with the Alpaca statue being moved independently

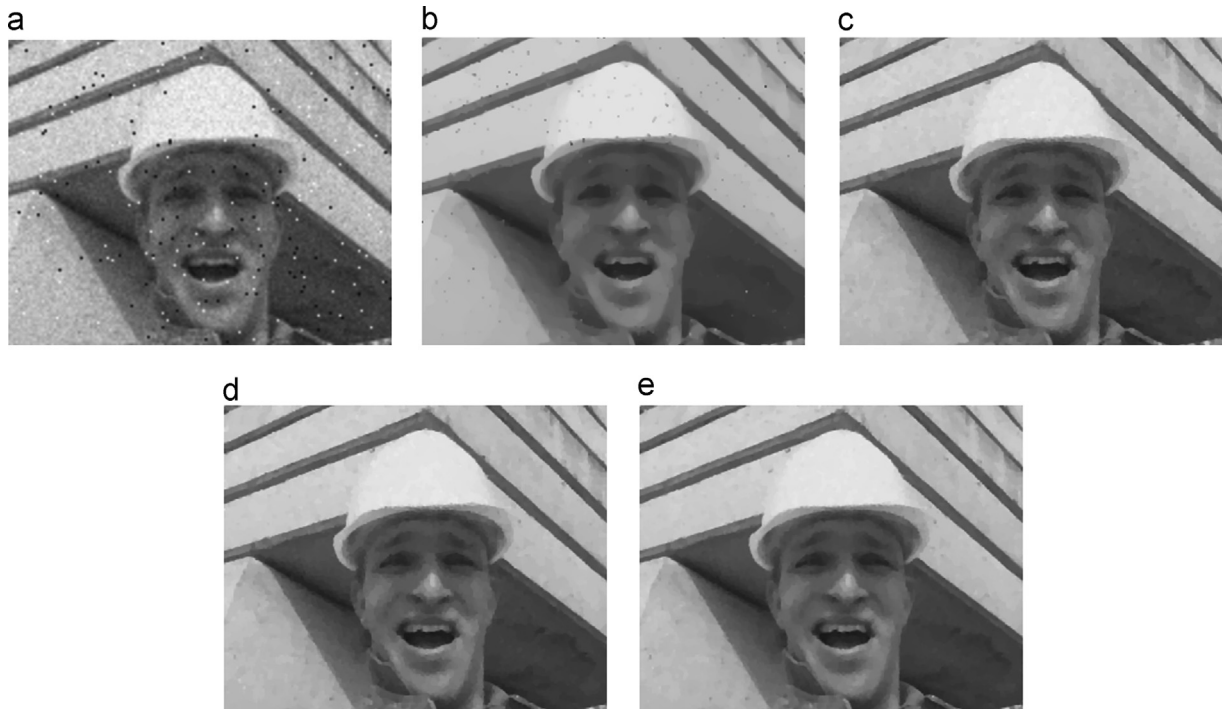


**Fig. 18.** Super-resolution results for the *Foreman* video sequence with “0.001+0.01”. (a) LR image, (b) result of L2, (c) result of L1, (d) result of M-estimator, and (e) result of the proposed method.

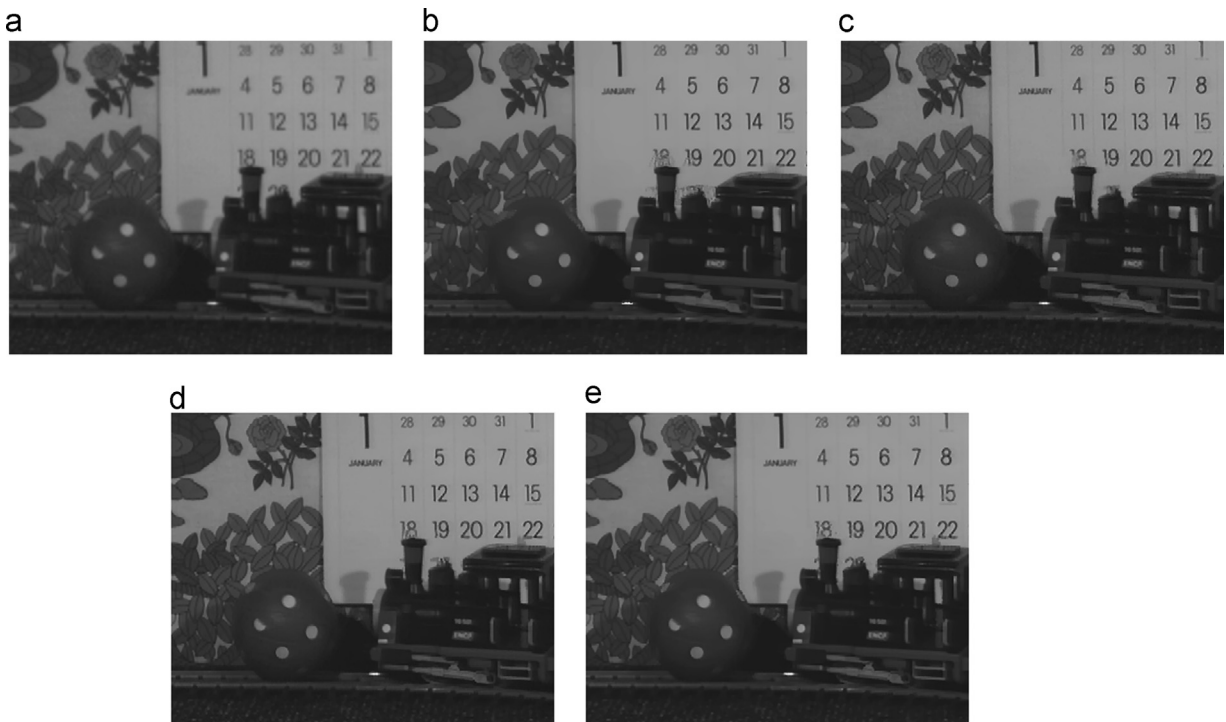


**Fig. 19.** Super-resolution results for the *Mobile and Calendar* video noiseless sequence. (a) LR image, (b) result of L2, (c) result of L1, (d) result of M-estimator, and (e) result of the proposed method.

in the last 10 frames. In our experiment, we used the last 10 frames to test the performance of the proposed method for the case of motion outliers and the unknown

compressed block artifact. The (unknown) camera PSF is assumed to be a  $3 \times 3$  Gaussian kernel with standard deviation equal to 1.

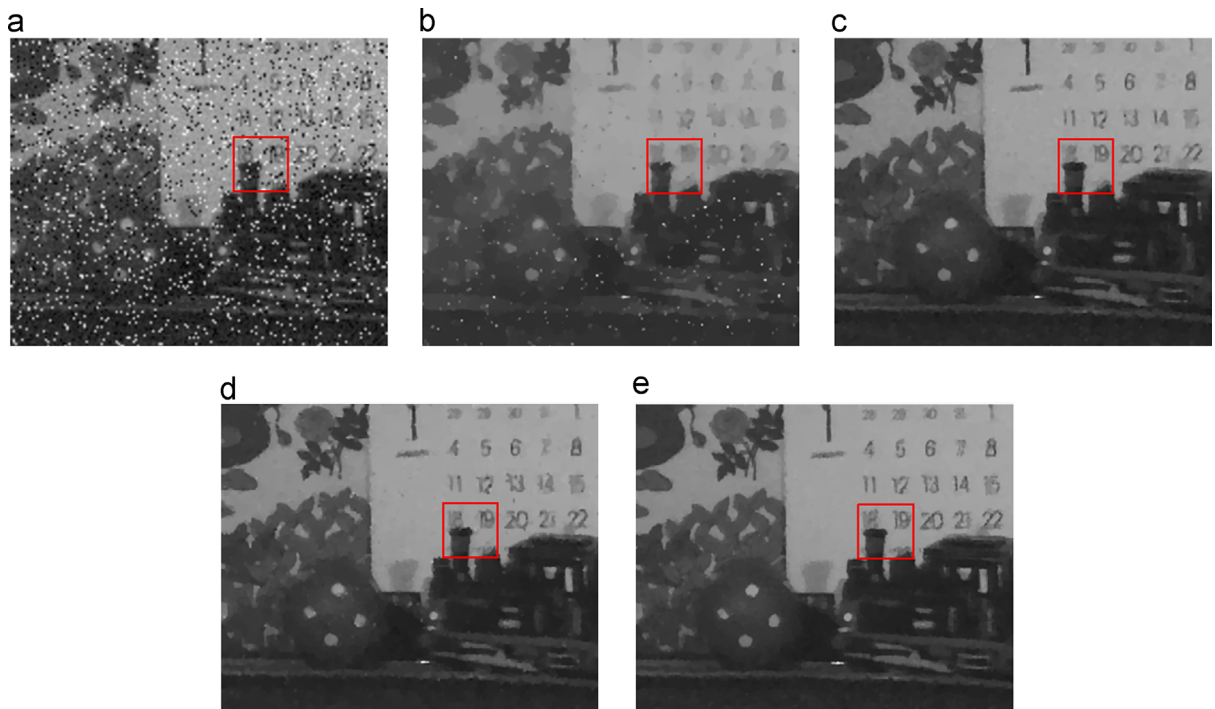


**Fig. 20.** Super-resolution results for the *Mobile and Calendar* video sequence with “0.001+0.1”. (a) LR image, (b) result of  $L_2$ , (c) result of  $L_1$ , (d) result of M-estimator, and (e) result of the proposed method. (For interpretation of the references to color in this figure caption, the reader is referred to the web version of this paper.)

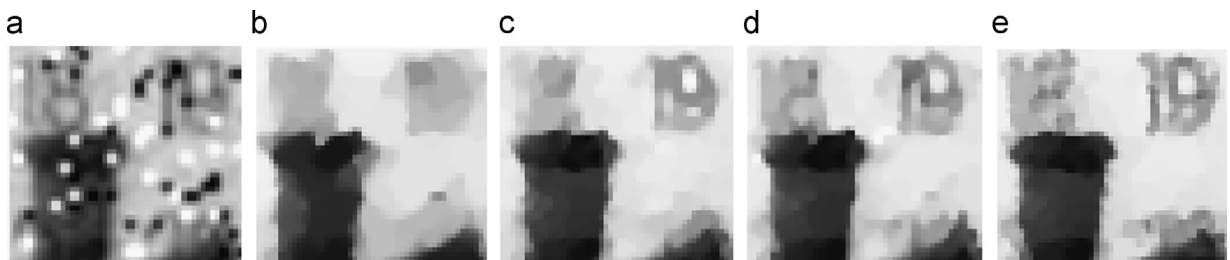


**Fig. 21.** The corresponding cropped images of Fig. 20.

**Table 4**  
Quantitative results of the *Foreman* image experiments.

Case	$L_2$	$L_1$	$L_2\_O$	$L_1\_O$	M-estimator	Manual	Adaptive
Noiseless ( $T = 0.1$ )							
PSNR	35.700	36.558	37.238	37.025	37.162	37.410	37.372
SSIM	0.943	0.959	0.959	0.959	0.959	0.957	0.961
Mixed (0.001+0.01) ( $T = 0.3$ )							
PSNR	30.748	32.760	30.652	32.668	33.120	33.459	33.474
SSIM	0.848	0.883	0.849	0.886	0.892	0.899	0.899

**Table 5**  
Quantitative results of the *Mobile and Calendar* image experiments.

Case	$L_2$	$L_1$	$L_2\_O$	$L_1\_O$	M-estimator	Manual	Adaptive
Noiseless ( $T = 0.3$ )							
PSNR	33.600	34.177	34.525	34.292	34.741	34.622	34.601
SSIM	0.897	0.913	0.911	0.914	0.918	0.911	0.911
Mixed (0.001+0.1) ( $T = 0.3$ )							
PSNR	24.634	25.651	23.980	28.404	28.257	29.435	29.440
SSIM	0.650	0.786	0.604	0.776	0.773	0.808	0.810

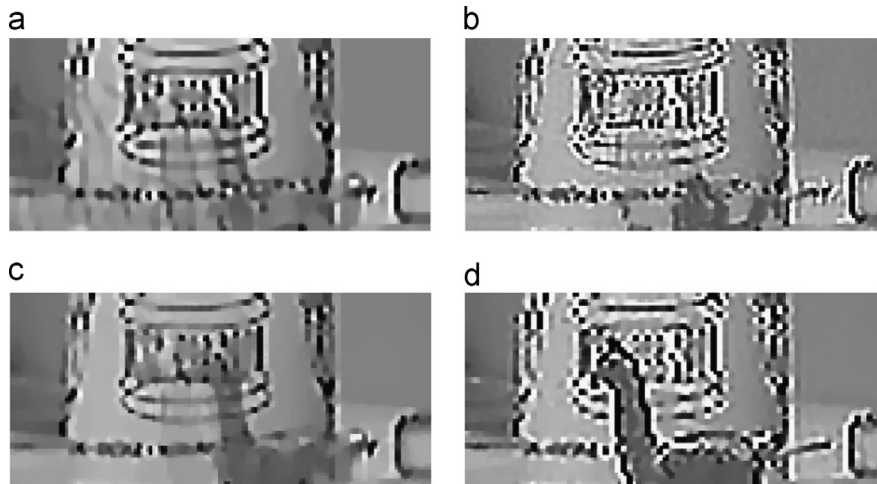


**Fig. 22.** The super-resolution results with an up-scaling factor of two. (a) Result of  $L2$ , (b) result of  $L1$ , (c) result of M-estimator, and (d) result of the proposed method.

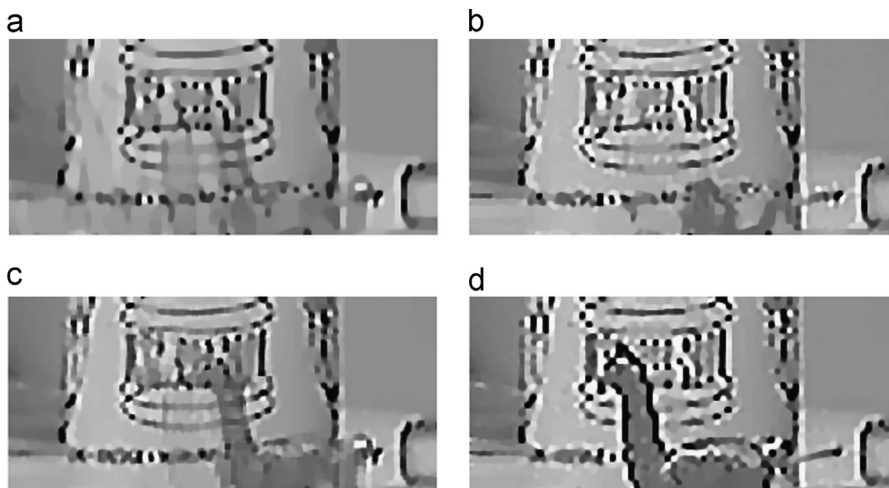


**Fig. 23.** The super-resolution results with an up-scaling factor of four. (a) Result of  $L2$ , (b) result of  $L1$ , (c) result of M-estimator, and (d) result of the proposed method.

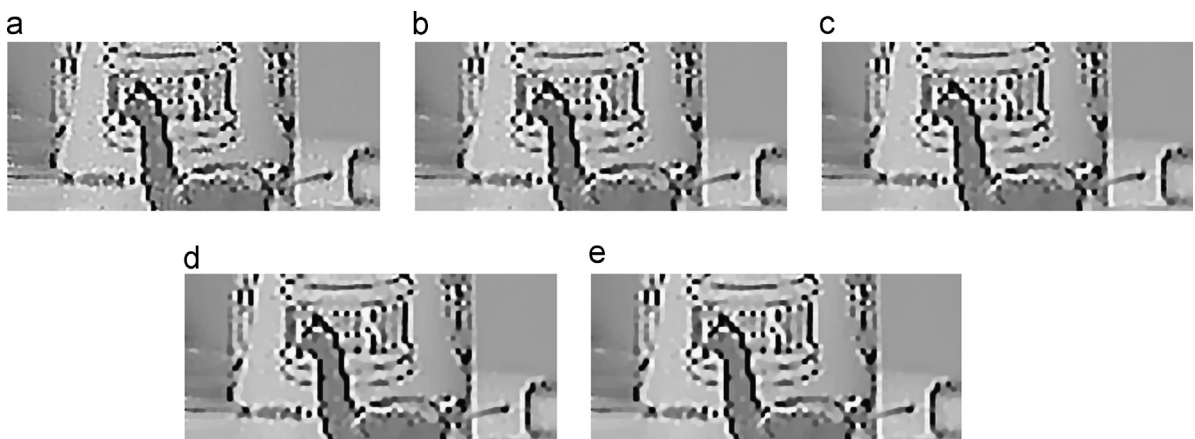


**Fig. 24.** The super-resolution results of proposed method with different regularization parameters. (a)  $\lambda=0.1$ , (b)  $\lambda=0.2$ , (c)  $\lambda=0.3$ , (d)  $\lambda=0.4$ , and (e)  $\lambda=0.5$ .

Since no ground truth is available for the real data, we could not evaluate the resulting HR frames with an objective quantitative measure such as PSNR or SSIM. However, the perceptual qualities illustrate the robustness of the proposed method with real video images. The results of the different models are given in Figs. 22 and 23. In order to observe the different behaviors of the super-resolution when dealing with compressed noise, we take the different scaling factors into account and show the reconstruction results with an up-scaling factor of two and four. It can be seen from Fig. 22 that the  $L_2$  norm gets the worst results, over-smoothing the details and being sensitive to the motion outliers.  $L_1$  also shows an unsatisfactory performance in the real compressed video sequence super-resolution, and almost misses the Alpaca statue. The M-estimator performs better, but the edges and texture are over-smoothed. Overall, it is apparent that the proposed method gets the most desirable results. When the scaling factor becomes larger, as shown in Fig. 23, the details become seriously blurred. However, the proposed method shows a relatively stable performance under the different scaling cases.

We also display Fig. 24 to show the influence of the different parameters. Although we adaptively determine the weight for the proposed model, the regularization parameter needs to be manually tuned. When we adopt small parameter values, the reconstructed images are affected by the remaining noise. As the parameter  $\lambda$  increases, the textures are missed to a certain extent, although the noise is filtered.

#### 4. Conclusion

Super-resolution reconstruction becomes more complicated when there is mixed corruption, such as mixed noise and/or multiple independent moving objects. To take the mixed degradation factor into account and solve it with a generalized model, we propose a locally adaptive norm super-resolution method to make use of the different norms' advantages for different types of model error. The proposed method adaptively selects a pixel-based  $L_1$ – $L_2$  norm, based on the detection results of the impulse noise and motion outliers. To simplify the procedure to tune parameters, a strategy for adaptive weight estimation for the data fidelity term is proposed. The proposed algorithm was tested in different cases, including synthetic mixed noise and a real video sequence with mixed noise and/or moving objects. The quantitative results, as well as the visual effects, confirm the method's stable performance. The adaptive parameter determination was also proven to be practical. Nevertheless, further work could be done to make improvements to the proposed method, such as increasing the accuracy of detection, reducing the error of motion estimation by the use of the video frames' redundant information. In addition, researchers have developed some proximal splitting methods [47,57,58] to improve the efficiency in solving nonlinear models. It is interesting to combine these advanced optimization methods with our framework. This will be included in our future work.

#### Acknowledgments

The authors would like to thank the editors and the anonymous reviewers for their valuable suggestions. This research is supported by Major State Basic Research Development Program (2011CB707105), National Natural Science Foundation of China (41271376), Program for Changjiang Scholars and Innovative Research Team in University (IRT1278) and Ph.D. Programs Foundation of Ministry of Education of China under Grant 20130141120001.

#### References

- [1] H.C. Liu, S.T. Li, H.T. Yin, Infrared surveillance image super resolution via group sparse representation, *Opt. Commun.* 289 (2013) 45–52.
- [2] D. Gleich, Markov random field models for non-quadratic regularization of complex SAR images, *IEEE J. Sel. Top. Appl. Earth Obser. Remote Sens.* 5 (3) (2012) 952–961.
- [3] Y. Zhang, A. Duijster, P. Scheunders, A Bayesian restoration approach for hyperspectral images, *IEEE Trans. Geosci. Remote Sens.* 50 (9) (2012) 3453–3462.
- [4] H. Zhang, L.P. Zhang, H.F. Shen, A super-resolution reconstruction algorithm for hyperspectral images, *Signal Process.* 92 (9) (2012) 2082–2096.
- [5] H.F. Shen, L.P. Zhang, B. Huang, et al., A MAP approach for joint motion estimation, segmentation, and super resolution, *IEEE Trans. Image Process.* 16 (2) (2007) 479–490.
- [6] M.H. Cheng, K.S. Hwang, J.H. Jeng, et al., Classification-based video super-resolution using artificial neural networks, *Signal Process.* 93 (9) (2013) 2612–2625.
- [7] R.Y. Tsai, T.S. Huang, Multi-frame image restoration and registration, *Adv. Comput. Vis. Image Process.* 1 (1984) 317–339.
- [8] S.P. Kim, N.K. Bose, H.M. Valenzuela, Recursive reconstruction of high resolution image from noisy undersampled multiframes, *IEEE Trans. Acoust. Speech Signal Process.* 38 (2) (1990) 1013–1027.
- [9] S.P. Kim, W.Y. Su, Recursive high-resolution reconstruction of blurred multiframe images, in: *International Conference in Acoustics, Speech, and Signal Processing, ICASSP-91*, vol. 4, 1991, pp. 2977–2980.
- [10] M. Irani, S. Peleg, Improving resolution by image registration, *CVGIP, Graph. Models Image Process.* 53 (3) (1991) 231–239.
- [11] Y. Zhang, Q. Zhou, An improved method for POCS superresolution image reconstruction, in: *International Conference on Electronics, Communications and Control*, 2011, pp. 4150–4153.
- [12] M.K. Ng, H.F. Shen, E.Y. Lam, et al., A total variation regularization based super-resolution reconstruction algorithm for digital video, *EURASIP J. Adv. Signal Process.* 2007 (2007) 074585.
- [13] H. Zhu, Y. Lu, Q.Z. Wu, Super-resolution image restoration by maximum likelihood method and edge-oriented diffusion, in: *Proceedings of the SPIE 6625, International Symposium on Photoelectronic Detection and Imaging 2007: Related Technologies and Applications*, 2008, 66250Y.
- [14] S.C. Park, M.K. Park, M.G. Kang, Super-resolution image reconstruction: a technical overview, *IEEE Signal Process. Mag.* 20 (3) (2003) 21–36.
- [15] S. Farsiu, M.D. Robinson, M. Elad, et al., Fast and robust multiframe super resolution, *IEEE Trans. Image Process.* 13 (10) (2004) 1327–1344.
- [16] B. Wohlberg, P. Rodriguez, AN 11-TV algorithm for deconvolution with salt and pepper noise, in: *IEEE International Conference on Acoustics, Speech and Signal Processing*, 2009, pp. 1257–1260.
- [17] S. Farsiu, M.D. Robinson, M. Elad, et al., Robust shift and add approach to superresolution, in: *SPIE's 48th Annual Meeting Optical Science and Technology*, 2003, pp. 121–130.
- [18] X. Zhang, E.Y. Lam, E.X. Wu, et al., Application of Tikhonov regularization to super-resolution reconstruction of brain MRI images, *Med. Imaging Inf.* (2008) 51–56.
- [19] R. Pan, S.J. Reeves, Efficient Huber–Markov edge-preserving image restoration, *IEEE Trans. Image Process.* 15 (12) (2006) 3728–3735.
- [20] Q.Q. Yuan, L.P. Zhang, H.F. Shen, Multiframe super-resolution employing a spatially weighted total variation model, *IEEE Trans. Circ. Syst. Video Technol.* 22 (3) (2012) 379–392.
- [21] A. Panagiotopoulou, V. Anastassopoulos, Super-resolution image reconstruction techniques: trade-offs between the data-fidelity and regularization terms, *Inf. Fusion* 13 (3) (2012) 185–195.

- [22] R.H. Chan, Y.Q. Dong, M. Hintermuller, An efficient two-phase L1-TV method for restoring blurred images with impulse noise, *IEEE Trans. Image Process.* 19 (7) (2010) 1731–1739.
- [23] M.E. Zervakis, A.N. Venetsanopoulos, Linear and nonlinear image restoration under the presence of mixed noise, *IEEE Trans. Circ. Syst.* 38 (1991) 258–272.
- [24] J.F. Cai, R.H. Chan, M. Nikolova, Fast two-phase image deblurring under impulse noise, *J. Math. Imaging Vis.* 36 (1) (2010) 46–53.
- [25] X. Zhou, C. Yang, W. Yu, Moving object detection by detecting contiguous outliers in the low-rank representation, *IEEE Trans. Pattern Anal. Mach. Intell.* 35 (3) (2013) 597–610.
- [26] P. Krämer, J.B. Pineau, J. Domenger, Local object-based super-resolution mosaicing from low-resolution video, *Signal Process.* 91 (8) (2011) 1771–1780.
- [27] S. Izadpanahi, H. Demirel, Motion based video super resolution using edge directed interpolation and complex wavelet transform, *Signal Process.* 93 (7) (2013) 2076–2086.
- [28] H. Song, D. Zhang, P. Wang, et al., AN adaptive L1–L2 hybrid error model to super-resolution, in: *IEEE International Conference on Image Processing (ICIP)*, 2010, pp. 2821–2824.
- [29] Y. Xiao, T.Y. Zeng, J. Yu, et al., Restoration of images corrupted by mixed Gaussian-impulse noise via l1-l0 minimization, *Pattern Recognit.* 44 (8) (2011) 1708–1720.
- [30] X.Y. Zeng, L.H. Yang, A robust multiframe super-resolution algorithm based on half-quadratic estimation with modified BTV regularization, *Digital Signal Process.* 23 (1) (2013) 98–109.
- [31] Y. Zhou, Z. Ye, Y. Xiao, A restoration algorithm for images contaminated by mixed Gaussian plus random-valued impulse noise, *J. Vis. Commun. Image Represent.* 24 (3) (2013) 283–294.
- [32] J. Zhang, R. Xiong, C. Zhao, et al., Exploiting image local and nonlocal consistency for mixed Gaussian-impulse noise removal, in: *IEEE International Conference on Multimedia and Expo (ICME)*, 2012, pp. 592–597.
- [33] J. Delon, A. Desolneux, A patch-based approach for removing mixed Gaussian-impulse noise, *SIAM J. Imaging Sci.* 6 (2) (2012) 1140–1174.
- [34] M. Jung, A. Marquina, L.A. Vese, Variational multiframe restoration of images degraded by noisy (stochastic) blur kernels, *J. Comput. Appl. Math.* 240 (2012) 123–134.
- [35] E. López-Rubio, Restoration of images corrupted by Gaussian and uniform impulsive noise, *Pattern Recognit.* 43 (5) (2010) 1835–1846.
- [36] C. Jin, M. Yan, S.W. Jin, An approach to remove impulse noise from a corrupted image, *J. Opt.* 15 (2) (2013) 025402.
- [37] R.R. Schultz, L. Meng, R.L. Stevenson, Subpixel motion estimation for super-resolution image sequence enhancement, *J. Vis. Commun. Image Represent.* 9 (1) (1998) 38–50.
- [38] O.A. Omer, T. Tanaka, Super-resolution based on region-matching motion estimation, *Vis. Commun. Image Process.* 6508 (2007) 65081.
- [39] T. Brox, J. Weickert, B. Burgeth, et al., Nonlinear structure tensors, *Image Vis. Comput.* 24 (1) (2006) 41–55.
- [40] Q.Q. Yuan, L.P. Zhang, H.F. Shen, Regional spatially adaptive total variation super-resolution with spatial information filtering and clustering, *IEEE Trans. Image Process.* 22 (2013) 2327–2342.
- [41] S. Lloyd, Least squares quantization in PCM, *IEEE Trans. Inf. Theory* 28 (2) (2006) 129–137.
- [42] X.L. Li, Y.T. Hu, X.B. G, et al., A multi-frame image super-resolution method, *Signal Process.* 90 (2) (2010) 405–414.
- [43] L.P. Zhang, Q.Q. Yuan, H.F. Shen, P.X. Li, Multiframe image super-resolution adapted with local spatial information, *J. Opt. Soc. Am. A* 28 (3) (2011) 381–390.
- [44] Y. Hu, M. Jacob, Higher degree total variation (HDTV) regularization for image recovery, *IEEE Trans. Image Process.* 21 (5) (2012) 2559–2571.
- [45] Z. Ren, C. He, Q. Zhang, Fractional order total variation regularization for image super-resolution, *Signal Process.* 93 (3) (2013) 2408–2421.
- [46] X. Zhang, M. Burger, X. Bresson, et al., Bregmanized nonlocal regularization for deconvolution and sparse reconstruction, *SIAM J. Imaging Sci.* 3 (3) (2010) 253–276.
- [47] P. Combettes, J.C. Pesquet, Proximal splitting methods in signal processing, *Fixed-Point Algorithms for Inverse Problems in Science and Engineering*, 2011, 185–212.
- [48] T. Goldstein, S. Osher, The split Bregman method for L1-regularized problems, *SIAM J. Imaging Sci.* 2 (2) (2009) 323–343.
- [49] S. Boyd, N. Parikh, E. Chu, et al., Distributed optimization and statistical learning via the alternating direction method of multipliers, *Found. Trends Mach. Learn.* 3 (1) (2011) 1–122.
- [50] P. Rodriguez, B. Wohlberg, Efficient minimization method for a generalized total variation functional, *IEEE Trans. Image Process.* 18 (2) (2009) 322–332.
- [51] D. Bertaccini, R.H. Chan, M. Serena, et al., An adaptive norm algorithm for image restoration, *Scale Space and Variational Methods in Computer Vision*, 6667, 2012, 194–205.
- [52] C. Vogel, M. Oman, Iterative methods for total variation denoising, *SIAM J. Sci. Comput.* 17 (1) (1996) 227–238.
- [53] Z. Wang, A. Bovik, H. Sheikh, Image quality assessment: from error visibility to structural similarity, *IEEE Trans. Image Process.* 13 (4) (2004) 600–612.
- [54] Z. Wang, A. Bovik, Mean squared error: love it or leave it: a new look at signal?delity measures, *IEEE Signal Process. Mag.* 26 (1) (2004) 98–117.
- [55] D. Capel, A. Zisserman, Computer vision applied to super resolution, *IEEE Signal Process. Mag.* 20 (3) (2003) 75–86.
- [56] S.M. Prabhu, A.N. Rajagopalan, Unified multiframe super-resolution of matte, foreground, and background, *J. Opt. Soc. Am. A* 30 (8) (2013) 1524–1534.
- [57] P.L. Combettes, V.R. Wajs, Signal recovery by proximal forward-backward splitting,, *Multiscale Model. Simul.* 4 (4) (2005) 1168–1200.
- [58] P.L. Combettes, J.-C. Pesquet, A proximal decomposition method for solving convex variational inverse problems,, *Inverse Probl.* 24 (6) (2008) 065014.